Elsevier Editorial System(tm) for Chemical Geology

Manuscript Draft

Manuscript Number:

Title: Modeling sulfate reduction and anaerobic oxidation of methane contributions to pH and CaCO3 saturation: are seep carbonates quantitative proxies of CH4 leakage?

Article Type: Research paper

Keywords: Seep carbonate; anaerobic oxidation of methane; early diagenesis; sulfate reduction; carbonate saturation; reaction transport modeling

Corresponding Author: Dr. Jean-Philippe Blouet, Ph.D.

Corresponding Author's Institution: University of Fribourg

First Author: Jean-Philippe Blouet, Ph.D.

Order of Authors: Jean-Philippe Blouet, Ph.D.; Arndt Sandra, professor; Patrice Imbert; Pierre Regnier

Abstract: Seep carbonates tell us where and when CH4-charged fluids escaped from the subsurface, thus providing qualitative information to reconstruct the activity of petroleum systems. The potential of seep carbonates as quantitative proxies for the amount of CH4 leaked, however, remains largely unexplored, which limit their applicability as exploration tools. This paper tackles the quantification of the CH4 flux - seep carbonate relationship by simulating the coupled sedimentary carbon (C) - sulfur (S) cycles in a reaction-transport modeling (RTM) framework. We first establish a theoretical basis demonstrating that the stoichiometry of diagenetic reactions and the ambient pH of pore waters are the main drivers of the rate of change in the saturation state of carbonate minerals (ΩCal), while the concentrations of total dissolved inorganic carbon and sulfide are only of secondary importance. It results that anaerobic oxidation of methane (AOM) is the main driver of carbonate precipitation, while organoclastic sulfate reduction (SR) has a minor impact. We further show that SR mostly drives carbonate dissolution, but can also contribute to precipitation when pH is low (<7-7.1). The RTM simulations reveal that an increase in upward fluid flow triggers an intensification of peak AOM rates, associated to a shallowing and thinning of the zone of carbonate precipitation. Such behavior leads to an almost linear relationship between the amount of carbonate precipitated and flux of CH4 (nCH4 = 3.3-5.2 * nCaCO3), until, eventually, full cementation occurs. We thus define a "quantitative domain" at moderate fluid flow and a "threshold domain" at high fluid velocities, where full cementation solely provides a lower bound estimate of the amount of CH4 leaked. We also show that in contrast to a traditional view of seep carbonate formation mainly controlled by venting activity, sedimentation rate and water depth also play major roles, via their control on residence time and saturation concentration of CH4, respectively. The interpretation of vertical seep carbonate stacks should thus not solely focus on changes in fluid flow, but also consider changes in sedimentation rate and/or water depth.

Suggested Reviewers: Maciej Bojanowski associated professor
Polish Academy of Sciences
mbojan@twarda.pan.pl
specialist of carbonate concretions

Giovanni Aloisi
institut de physique du globe de paris
aloisi@ipgp.fr
specialiste of the reaction of anaerobic oxydation of methane in marine sediment and of reaction transport modeling.

Ivano Aiello
Moss Landing Marine Laboratories
iaiello@mlml.calstate.edu
marine geologist, specialist of microbial activity at modern seep sites, and of fossil seep sites.

patrick meister
Universität Wien
patrick.meister@univie.ac.at
specialist of authigenic mineral precipitation and reaction transport modeling

Laura Wehrmann
Max Planck Institute for Marine Microbiology
laura.wehrmann@stonybrook.edu
specialist of early diagenetic processes, and the carbon and sulfur cycles in marine sediments

Reinhard Weidlich
University of Fribourg
reinhard.weidlich@unifr.ch
chemist currently working on seep carbonate offshore Palestine.

Volker Liebetrau
GEOMAR
vliebetrau@geomar.de
specialist of sea floor diagenesis in relation with methane leakage

Alexandra Turchyn
University of Cambridge
atur07@esc.cam.ac.uk
specialist of biogeochemical reaction in marin sediments

Eric Gaucher
Total SA
eric.gaucher@total.com
specialist of water-rock interaction and petroleum exploration

Research Data Related to this Submission

There are no linked research data sets for this submission. The following reason is given:
No data was used for the research described in the article

Cover Letter

Dear professor Dong,

We are pleased to submit an original research article entitled "Modeling sulfate reduction and anaerobic oxidation of methane contributions to pH and $CaCO_3$ saturation: are seep carbonates quantitative proxies of CH_4 leakage?" for consideration by Chemical Geology.

In this paper, we tackle the quantification of the CH_4 flux - authigenic carbonate relationship in marine sediments by simulating the coupled sedimentary carbon – sulfur cycles in a reaction-transport modelling framework. It results that the reaction of anaerobic oxidation of methane (AOM) is the main driver of carbonate precipitation, and that the CH_4 flux almost linearly scales to the amount of precipitated carbonate, till full cementation occurs. The carbonates observed at seep sites can thus be used a quantitative indicators for CH_4 migrating through sediments, establishing seep carbonates as proxies to reconstruct the activity of the 'plumbing system' of sedimentary basins.

We believe that this manuscript is appropriate for publication in Chemical Geology because it establishes a theoretical basis demonstrating that the stoichiometry of diagenetic reactions and the ambient pH of pore waters are the main drivers of the rate of change in the saturation state of carbonate minerals, which is of interest for the geochemistry community. The broad applicability of the results may extend the impact of this article to the wider geology community.

We confirm that this work is original and has not been published elsewhere, nor is it currently under consideration for publication elsewhere.

Thank you for your consideration of this manuscript.
Sincerely,

Jean-Philippe BLOUET,
Université Libre de Bruxelles, Belgium
jeanphilippe.blouet@gmail.com

Modeling sulfate reduction and anaerobic oxidation of methane contributions to pH and $CaCO_3$ saturation: are seep carbonates quantitative proxies of CH_4 leakage?

Jean-Philippe Blouet[1] ; Sandra Arndt[1] ; Patrice Imbert[2] ; Pierre Regnier[1]

[1]Department of Geosciences, Environment and Society, Université Libre de Bruxelles, Avenue Franklin Roosevelt 50, 1050 Brussels, Belgium

[2]Centre Scientifique et Technique Jean Feger, Total, Avenue Larribau, 64000 Pau, France

Corresponding author:

Jeanphilippe.blouet@gmail.com

Emails of co-autors:

Sandra.Arndt@ulb.be

Pierre.Regnier@ulb.ac.be

patrice_imbert@msn.com

Abstract

Seep carbonates tell us where and when CH_4-charged fluids escaped from the subsurface, thus providing qualitative information to reconstruct the activity of petroleum systems. The potential of seep carbonates as quantitative proxies for the amount of CH_4 leaked, however, remains largely unexplored, which limit their applicability as exploration tools. This paper tackles the quantification of the CH_4 flux - seep carbonate relationship by simulating the coupled sedimentary carbon (C) – sulfur (S) cycles in a reaction-transport modeling (RTM) framework. We first establish a theoretical basis demonstrating that the stoichiometry of diagenetic reactions and the ambient pH of pore waters are the main drivers of the rate of change in the saturation state of carbonate minerals (Ω_{Cal}), while the concentrations of total dissolved inorganic carbon and sulfide are only of secondary importance. It results that anaerobic oxidation of methane (AOM) is the main driver of carbonate precipitation, while organoclastic sulfate reduction (SR) has a minor impact. We further show that SR mostly drives carbonate dissolution, but can also contribute to precipitation when pH is low (<7-7.1). The RTM simulations reveal that an increase in upward fluid flow triggers an intensification of peak AOM rates, associated to a shallowing and thinning of the zone of carbonate precipitation. Such behavior leads to an almost linear relationship between the amount of carbonate precipitated and

flux of CH_4 ($nCH_4 = 3.3\text{-}5.2 * nCaCO_3$), until, eventually, full cementation occurs. We thus define a "quantitative domain" at moderate fluid flow and a "threshold domain" at high fluid velocities, where full cementation solely provides a lower bound estimate of the amount of CH_4 leaked. We also show that in contrast to a traditional view of seep carbonate formation mainly controlled by venting activity, sedimentation rate and water depth also play major roles, via their control on residence time and saturation concentration of CH_4, respectively. The interpretation of vertical seep carbonate stacks should thus not solely focus on changes in fluid flow, but also consider changes in sedimentation rate and/or water depth.

Keywords

Seep carbonate; anaerobic oxidation of methane; early diagenesis; sulfate reduction; carbonate saturation; reaction transport modeling

1. Introduction

Seep carbonates are diagenetic features associated with the upward migration of hydrocarbons to the seabed at cold seeps, in particular methane (CH_4) (Hecker, 1985; Juniper and Sibuet, 1987). They often precipitate in the shallow subsurface, within the sulfate CH_4 transition zone (SMTZ), driven by the microbially mediated anaerobic oxidation of hydrocarbons coupled to the reduction of pore water sulfate, that produces DIC and alkalinity, raises the pH and increase the concentration of carbonate ions until the saturation state of porewaters with respect to calcium carbonate minerals (Ω_{Cal}) is reached, triggering precipitation. Seep carbonates are thus the most obvious indicators of the discrete phenomenon of oil, gas, and hydrocarbon charged aqueous fluids leakage in the marine deposits and have been used as qualitative proxies to reconstruct the 'plumbing system' of sedimentary basins (Talukder et al., 2012).

For instance, observations of seep carbonate at the sea floor, complemented with acoustic (1-10 kHz) and high-resolution seismic data (1 - 50 Hz) can be used to reconstruct fluid circulation in the shallow seabed and are predominantly used in geohazard prevention, i.e. in the study of seafloor instability (Riboulot et al., 2015). On a million-year timescale, the vertical succession of seep carbonate bodies observed in seismic data (50-80Hz) has been used to reconstruct the history of hydrocarbon leakage (Ho et al., 2012, 2016, 2018 a, b). When hydrocarbon seepage is linked to the activity of an underlying petroleum system (sensu Magoon and Dow, 1994), information about seep carbonates can be combined with knowledge about the tectono-sedimentary context of their host basin, to help track migration pathways down to hydrocarbon source rocks, potentially identifying reservoirs and accumulations (Agirrezabala, 2009, 2015; Blouet et al., 2017). On a muti-millenial

timescale, seep carbonates have also been used to estimate the temporal evolution of benthic CH_4 efflux in the aftermath of a glaciation and its feedback on climate (Crémière et al., 2016). Seep carbonates are thus a unique tool that tell us where, when and how hydrocarbon-charged fluids escape(d) from the sediment. However, until present their potential as a quantitative indicator of hydrocarbon flux remains largely unexplored and is the focus of this paper.

Our ability to extract quantitative estimates of fluid flux from observed seep carbonates largely relies on the development of a quantitative framework such as reaction transport models (RTM). Since about three decades (e.g. Wang and Van Cappellen 1996, Soetaert 1996), integrated data-RTM approaches have been commonly used tool to disentangle and quantify the early diagenetic processes interplay. While modeling the complexity of anaerobic oxidation of oil compounds remains largely out of reach (e.g. Joye et al., 2004; Kleindienst et al., 2014), the reaction of anaerobic oxidation of CH_4 (AOM), catalyzed by a consortium of archaea and bacteria has been extensively studied and is comparably well understood (Boetius et al., 2000). Building on a large body of published RTM studies, Regnier et al. (2011) highlighted the differences in CH_4 and sulfate cycling between passive and active settings. Passive settings correspond to sea floor areas without significant advective CH_4 flow, the vast majority of the sea floor surface, while seep sites with advection of dissolved or gaseous CH_4 are typically found along continental margins. In passive settings, AOM is mostly fueled by in-situ biogenic CH_4 production below the zone of organoclastic sulfate reduction, which diffuses upcore and is subsequently oxidized by sulfate in the SMTZ. Any authigenic carbonate precipitated is such a passive setting is not diagnostic of the activity of a petroleum system (e.g. Lash, 2018). In contrast, in active settings, upward fluid flow supplies large amount of previously formed biogenic and/or thermogenic hydrocarbons, including CH_4, that migrate from deep geological reservoirs (Talukder, 2012). Regnier et al. (2011) showed that the depth-integrated AOM rate and the depth of the SMTZ can be directly linked to fluid flow velocities. Similarly, RTM studies of CH_4 seep sites in accretionary prisms offshore Oregon and offshore Costa Rica have highlighted that authigenic carbonate precipitation is largely controlled by fluid flow intensity and sedimentation rate (Luff and Wallman, 2003; Luff and al., 2004; Aloisi et al., 2004; Luff and al., 2005; Karaca et al., 2010, 2014). Those models successfully reproduced observed geochemical profiles and provided first quantitative insights into the link between authigenic carbonate precipitation and upward CH_4 flow. However, such local, site-specific knowledge cannot easily be extrapolated to other seep sites. Indeed, the impact of the variability in water depth, sedimentation rate, AOM kinetic rate constant and/or the intensity of macrofauna activity (i.e. bioturbation and bioirrigation) over the wide range of values observed in marine settings (Middelburg et al., 1997) has not yet been systematically investigated. In light of these knowledge gaps, this study aims at assessing the suitability of seep carbonates as quantitative proxies for

upward CH_4 fluxes. To do so, the full range of environmental controls on the coupled AOM-carbonate dynamics in active settings will be explored to answer the following specific research questions:

*Can we develop a quantitative, interpretative framework relating upward CH_4 flow, AOM rate and associated pH change, to carbonate precipitation?

* What are the dominant environmental controls on the coupled AOM-carbonate dynamics in active settings?

* Under which conditions are seep carbonates suitable quantitative proxies for active CH_4 flow?

The first part of this paper builds the theoretical framework that describes the contribution of individual biogeochemical reactions on the rate of change in pH and Ω_{Cal}. We then simulate a typical passive and a typical active setting to identify the main drivers of calcium carbonate precipitation in these contrasted environments. Depth-integrated reaction rates are compared with previously published values and help benchmark the model. The quantitative relationship between the flux of CH_4 and the amount of carbonate precipitated is then explored systematically across the typical gradient of benthic habitats observed around fluid vents. Variations in the amount of carbonate precipitated as a function of water depth and sedimentation rate are quantitatively established, while uncertainties arising from the poorly constrained rate constant of AOM (k_{AOM}), bioturbation and bioirrigation intensities are also assessed. The ability of the model to reproduce observations is discussed, highlighting current model limitations. Finally, the novel quantitative framework is applied to approximate the growth rate of seep carbonate concretions, and a representative example of seep carbonate body observed on seismic data is used as a case study to reconstruct CH_4 seepage history over geological time.

2. Methodology

2.1. Modeling strategy

Here, we use the Biogeochemical Reaction Network Simulator (BRNS, Regnier et al., 2002; Aguilera et al., 2005) to quantitatively explore the mechanisms and drivers of authigenic carbonate precipitation at steady state using sets of environmental conditions corresponding to a passive regime (i.e. no upward advective fluid flow) and active regimes (i.e. upward fluid flow) with a flux, q, of 5 cm/yr, 10 cm/yr, 20 cm/yr, and 100 cm/yr. The lower range of fluid flow values is typically obtained by parameter fitting to geochemical profiles measured in the sediment cores at seep sites (Regnier et al., 2011), while the upper range, and even values several orders of magnitude higher, is more often obtained by direct measurement of the fluid flow during punctual sea floor observations (Henry et al., 1992, 1996; O'Hara et al., 1995; Tryon et al., 1999, 2002; Tryon and Brown, 2004).

In BRNS, the sea floor sediment is conceptualized as a one-dimensional (1D) system, with an upper boundary corresponding to the sea floor (z_0), and the lower boundary at a given depth (z_{max}). The condition of conservation of mass through this 1D system is described by the general diagenetic equation of Berner (1980):

$$\frac{\partial \xi_i C_i}{\partial t} = \frac{\partial^2 (D_i + Db) C_i}{\partial z^2} - \frac{\partial (\xi_i v C_i)}{\partial z} + \alpha (C_i(0) - C_i) + \xi_i \sum_j s_i^j R_j \qquad (1)$$

Where C_i is the concentration of specie *i*, *t* is time, *z* denotes the depth within the sediment, and ξ_i is the volume fraction in which the concentration of specie *i* is defined. The concentration of dissolved species is usually given in units of mass per unit volume of pore fluid, ξ_i = porosity (φ); likewise, for solid species, the concentration is usually expressed per unit volume of solid sediment, $\xi_i = (1- \varphi)$. D_i is the effective molecular diffusion coefficient of specie *i*, Db is the bioturbation coefficient ν is the advection velocity, α is the bioirrigation coefficient, $C_i(0)$ is the concentration at the sea floor, s_i^j is the stoichiometric coefficient of production/consumption of the specie *i* by the reaction *j*, and R_j is the rate of the reaction *j*. For solid species, D_i and α are equal to 0 and $v_{(solids)}$ is equal to the burial rate ω, that is, the sedimentation rate at the seafloor (ω_0) corrected for compaction with depth into the sediment (equation 2). Db acts on both solid and solute species and control their mixing in the upper, bioturbated layer of the sediment. For dissolved species $v_{(solutes)}$ corresponds to the velocity of fluid advected upward (q) and pore water expulsion by compaction, minus the downward burial component of the solid sediment frame (ω) (equation 3). Note that dissolved species can also be efficiently transported near the sediment surface through bioirrigation.

$$v_{(solids)} = \omega_0 \frac{(1-\varphi_0)}{(1-\varphi_z)} \qquad (2)$$

$$v_{(solutes)} = \omega_0 \frac{(1-\varphi_0)*\varphi_\infty}{(1-\varphi_\infty)*\varphi_z} + q \qquad (3)$$

The porosity depth law (equation 4) is applied to account for compaction:

$$\varphi_z = \varphi_\infty + (\varphi_0 + \varphi_\infty) * e^{(-z*attpor)} \qquad (4)$$

where φ_0 is the porosity at the sea floor, φ_∞ is the porosity at great depth and attpor is an attenuation coefficient determining the rate at which the porosity decreases with depth.

Resolution of equation 1 requires boundary conditions at the seafloor (z_0) and bottom of the model domain (z_{max}), which are presented in section 3.2.2. Details about the numerical solution of the coupled system of equations (1) for all species i can be found in Regnier et al. (2002). The spatial discretization is performed along an irregular grid, and z_{max} is reduced as much as possible to

optimize the simulation time as long as the position of lower boundary conditions have no noticeable impact on the reaction rates in the SMTZ. For q spanning from 0 to 20 cm/yr, the grid is composed of 202 nodes with a spacing increasing from 0.1 cm at the sea floor to 2.5 cm at a z_{max} of 300 cm. For q=100 cm/yr, the numerical solution of the very sharp concentration gradients imposes a grid spacing twice thinner, with 250 nodes covering a sediment layer with z_{max} equal to 100 cm. Simulations are carried until steady state is reached using a maximum time step of 0.005 yr for all runs.

2.2. Set-up for the baseline Model

The BRNS is applied to simulate the diagenetic dynamics in a shelf and slope setting subject to the seepage of a typical connate fluid equilibrated with a gas reservoir. This section describes the reaction network (Table 1 and 2), the model parameters and boundary conditions (Table 3 and 4) and the dependency of several key parameters to the fluid flow (Table 5).

2.2.1. Reaction network

The reaction network implemented in BRNS, with details on stoichiometries, kinetic and thermodynamic constants, is described in Table 1 and 2. Kinetic reactions include organoclastic sulfate reduction (SR, coupled to particulate organic carbon (POC) degradation), methanogenesis (Meth), anaerobic oxidation of CH_4 (AOM, or sulfate-reduction coupled to CH_4 oxidation), calcite precipitation and dissolution, which are the most influential diagenetic reactions in active settings (e.g. Dale et al., 2009). The model resolves the concentration of redox sensitive species as well as the concentration of each species contributing to the total dissolved inorganic carbon (Tc), sulfide (Ts), borate (Tb), alkalinity (Ta) and water systems independently. Acid-base equilibriums are assumed for the latter species and are thus controlled via thermodynamic constants corrected for pressure (P), temperature (T), and salinity (S) (Millero, 1995).

The degradation of organic matter, simplified as $CH_2O(NH_3)_y$ where y=16/106, is described by the reactive continuum model (Boudreau and Ruddick, 1991), assuming a continuous distribution of organic matter compounds over a reactivity spectrum. The overall rate of organic matter degradation, R_{POC}, decreases according the burial time (age), and is thus controlled by the decrease in organic matter concentration, as well as the factors that control the age of the buried sediment layer, i.e. the sedimentation rate of burial, and bioturbation within the bioturbated layer.

$$R_{POC}(z) = (nu/ (a + age (z))) * CH_2O(NH_3)_y(z) \quad (5)$$

where a and nu are depth-independent parameters that determine the distribution of organic matter over the reactivity spectrum, 10 yr and 0.125 [-] respectively, which correspond to the typical reactivity of marine organic matter on shelf and slope environments (Arndt et al., 2013). POC degradation reactions proceed in the order of decreasing free energy yield (e.g. Thullner and Regnier,

2019 and references therein) in such a way that methanogenesis is inhibited by the presence of SO_4. R_{POC} is thus partitioned in two primary redox reactions (Table 1): sulfate reduction (R_{SR}), followed by methanogenesis (R_{Meth}), with $R_{POC\,(z)} = R_{SR\,(z)} + R_{Meth\,(z)}$. CH_4 produced by methanogenesis inside the model, or transported through the lower boundary from a deeper source, is susceptible to migrate by diffusion and advective fluid flow up to the sulfate bearing sediment layer, leading to AOM (Table 1). AOM is a classical secondary redox reaction whereby reduced products of POC degradation (in this case, CH_4) are oxidized as they move up the sediment column and encounter energy yielding oxidants (in this case, SO_4^{2-}). During AOM, two mol-equivalents of alkalinity are generated per mol of DIC produced (table 1), leading to an increase in pH and thus an increase in the saturation state with respect to carbonate minerals (Luff et al., 2004; Jourabchi et al., 2005).

The saturation state of calcium carbonates (Ω_{Cal}) is controlled by the solubility product for calcite and the apparent thermodynamic constant K^*_{spCal} which is a function of P, T and S (Millero, 1995):

$$\Omega_{Cal} = \frac{[Ca^{2+}][CO_3^{2-}]}{K^* spCal} \qquad (6)$$

Given the diversity of calcium carbonate mineralogy and habitus observed at seep sites (Campbell, 2006; Blouet et al., 2017), and the lack of knowledge on parameters that control this variability, especially in micro-environments influenced by microbial activity (Burton, 1993; Railsback and Bruce, 2006; Kaczmarek et al., 2017), it is considered pointless to include several calcium carbonate species in the model. We thus use calcite as our representative carbonate mineral and the rate of calcite precipitation (Table 1), $R_{CalPrec}$, is assumed to be linearly proportional to the saturation state, Ω_{Ca} (Luff and Wallmann, 2003; Luff et al., 2004; Luff et al., 2005), with a kinetic constant set to a large value ($K_{CalPrec}$= 0.1 mol/cm^3/yr), similarly to Luff et Wallman (2003) and Wallmann et al. (2006). The rate of calcite dissolution, $R_{CalDiss}$, is also linearly proportional to the saturation state but is also assumed to depend on the amount of $CaCO_3$, the latter factor being used as surrogate for the availability of reactant surface (Table 1). This approach sets the dissolution rate to 0 if no calcite is present (Jourabchi et al., 2005).

The composition of sea water used to define upper boundary conditions for the baseline run (see section 3.2.2) leads to $\Omega_{Cal}(z_0)$ =2.33, lower than the kinetic oversaturation threshold commonly accepted for calcite precipitation to occur on the sea floor (Morse, 2003). This kinetic oversaturation threshold, however, is poorly known in quantitative terms and remains speculative, especially in diagenetic environments. To account for the common observation of no calcite cementation right at or just below the seafloor, and as sulfate reduction typically reduces rapidly Ω_{Cal} to values < 1 for the sea water pH defined in the model (Gallagher et al., 2014), precipitation is set to 0 from the sea floor down to the depth z_{diag} where diagenetic reactions, in particular AOM, lead to $\Omega_{Cal}(z_{diag})$ again greater

than 1. z_{diag} may be considered as the boundary between the very shallow sediment, invaded by slightly modified sea water, and the diagenetic domain where internal processes substantially impact the pore water composition. Below z_{diag}, precipitation and dissolution are allowed as soon as Ω_{Cal} is different from 1.

2.2.2. Prescribed model parameters and boundary conditions

The baseline model is first established at the typical self-break water depth of 200 m, and for a sedimentation rate (w) set to 0.1 cm/yr, which corresponds to the typical order of magnitude of sedimentation at such depth according to Middelburg et al. (1997). We then explore the entire parameter space of water depth and w values for shelf and slope sediments, using water depth = 10, 100, 200, 500, 1000 m and w = 1, 0.5, 0.2, 0.1, 0.01, 0.001 cm yr^{-1}.

The porosity profile is constant for all our simulations and fitted to values measured on the Angola passive continental margin (φ_{z0}=0.92; φ_{∞}=0.8; attpor= 0.15; Eric Cauquil, personal communication), a prolific hydrocarbon province rich in seep sites (e.g. Ho et al., 2012, 2018a, b). The molecular diffusion coefficients D_i for each specie i are adjusted for temperature, salinity and sediment tortuosity (Boudreau, 1997):

$$Di=((0.95-0.001*S)*D_i0*(1+fT*T))/(1-\ln(\phi^2) \quad (6)$$

Where $D_{i,0}$ is the molecular diffusion coefficient at 0°C listed in Table 3, T (°C) is the temperature, S (‰ wt) is the salinity and fT is an empirical correction for the effect of temperature.

At the upper boundary of the model (Table 4), fixed concentrations of a typical seawater (Arndt et al., 2011) are assigned to the solute species (Dirichlet condition). The concentration of CH_4 in particular is set to 0, accounting for instantaneous dilution of the connate fluid in the highly turbulent ocean reservoir. The sedimentation of solid species is specified as a depositional flux (Robin condition). As Tc, Ts, Tb, Ta and pH are dependent variables, and as Tc is usually difficult to measure in seawater, Ts, Tb, Ta and pH are specified variables while Tc is computed consistently from the specified variables.

To constrain the composition of the connate fluid at the lower boundary, the model is first run with all parameter values identical to the baseline setting with q=0 and Neumann conditions (i.e. zero concentration gradient) assigned at the lower boundary for all species, but in this case down to a depth where the reactivity of the organic matter $R_{POC}(z)$ is reduced to 1/1000 of its value at the sea floor, i.e. down to a depth where the species concentrations are almost constant with depth. This condition is achieved at a depth of about 3 m. The resulting connate fluid composition is representative of typical methanogenic conditions (Table 4), strongly enriched in CH_4, NH_4^+, sulfides, and dissolved carbonate species (almost entirely HCO_3^- and CO_2 due to the relatively low pH) compared to seawater. Due to the high kinetic rates of calcite precipitation/dissolution imposed, the connate fluid is very near equilibrium with calcite. Because the thermodynamic constants depend on

pressure, the composition of the connate fluid is adjusted following the above described procedure for each water depth when exploring the sensitivity of the model to water depth. The concentration of dissolved CH_4 was calculated considering equilibrium with the gas phase ($[CH_4]_{sat}$) at the given P, T and S according to the formula of Soreide and Whitson (1992). To reproduce the seepage, the concentrations of the connate fluid computed above are specified as Dirichlet conditions at depth z_{max}, which are then transported upward through the model by active fluid flow. The solid species remain constrained by Neumann conditions at the lower boundary of the baseline model. As such, the advective flux from below transports the dissolved species into the model. In the passive setting, the composition of the connate water diffuses upward and represents the case of a fluid accumulation trapped in the sediment at the bottom of the model domain.

2.2.3. Model parameters related to the fluid flow

Numerous studies have shown that the upward flux of CH_4 impacts the composition and density of the chemosynthetic fauna living at seepage sites. As a result, the fauna typically arranges in concentric habitats around seep sites (Juniper and Sibuet, 1987; Barry et al., 1997; Sibuet and Olu, 1998; Levin 2003, 2005; Fischer et al., 2012). The central area is usually covered by bacterial mats and devoid of macro-organisms, while the periphery is covered by a dense population of chemosynthetic animals, including benthic and endobenthic bivalves (Kiel, 2010). To mimic these features in our simulations, a passive sea floor environment with a sparse faunal density is imposed for q=0 cm yr^{-1}, a peak of macrofaunal activity is inferred at q=5 cm yr^{-1} and a bacterial mat is assumed for q≥20 cm yr^{-1}.

The bioturbation coefficient, Db, and the depth of bioturbation, Db_{zbiot}, defining the portion of the sediment below the sea floor where biological mixing occurs, are poorly constrained at seep sites. Following many previous modeling studies (e.g. Thullner et al., 2009; Hülse et al., 2018), the sea floor value Db_0 for q = 0 cm yr^{-1} is assumed to be a function of sea floor depth according to the empirical relationship of Middelburg et al., (1997), and Db_{zbiot} is set constant at 10 cm. A high Db_0 value (100 cm^2 yr^{-1}, Solan et al., 2019) is set for q=5 cm yr^{-1} while it is set to 0 in the bacterial mat environments. The bioirrigation coefficient, α (yr^{-1}), is calculated from the bioirrigation coefficient at the sediment surface, α_0, and is assumed to decrease exponentially below the sea floor (Thullner et al., 2009):

$$\alpha = \alpha_0 * e^{(-z/zirr)} \quad (7)$$

where zirr, the depth of bioirrigation, largely unknown at seep sites is set to a constant value of 3.5 cm. This value is typical for shelf sediments (Solan et al.; 2019) and leads to a depth where bioirrigation intensity is half that at the seafloor of 2,4 cm. The sea floor value α_0 is set to 1 yr^{-1} when q=0, is maximal at 50 yr^{-1} when q=5 cm yr^{-1} and is 0 for the bacterial mat environments.

A review by Regnier et al. (2011) established that the rate constant for AOM, k_{AOM}, is also strongly correlated to q, due to the development of the microbial population that catalyze the AOM reaction (Dale et al., 2006, 2008; Nauhaus et al., 2007). Based on Regnier et al. (2011), k_{AOM} is set to 10^5 cm^3 mol^{-1} yr^{-1} in the passive setting while the following linear relationship is used in active settings:

$$k_{AOM} = 2{,}7*10^5*q \quad (8)$$

Therefore, microbial and fauna dependent variables, that is, the rate constant for AOM, the bioturbation and the bioirrigation coefficients, are all related to q (Table 5). Quantitative data used to establish empirical relationships are presented in Fig 1. Given the significant uncertainties in these empirical relationships, the sensitivity of the model to k_{AOM}, Db and α will be further evaluated through a sensitivity study (Table 6, section 3.3.2), keeping all parameters but the studied one constant at their mean value, while also keeping the water depth and the sedimentation rate at their baseline value.

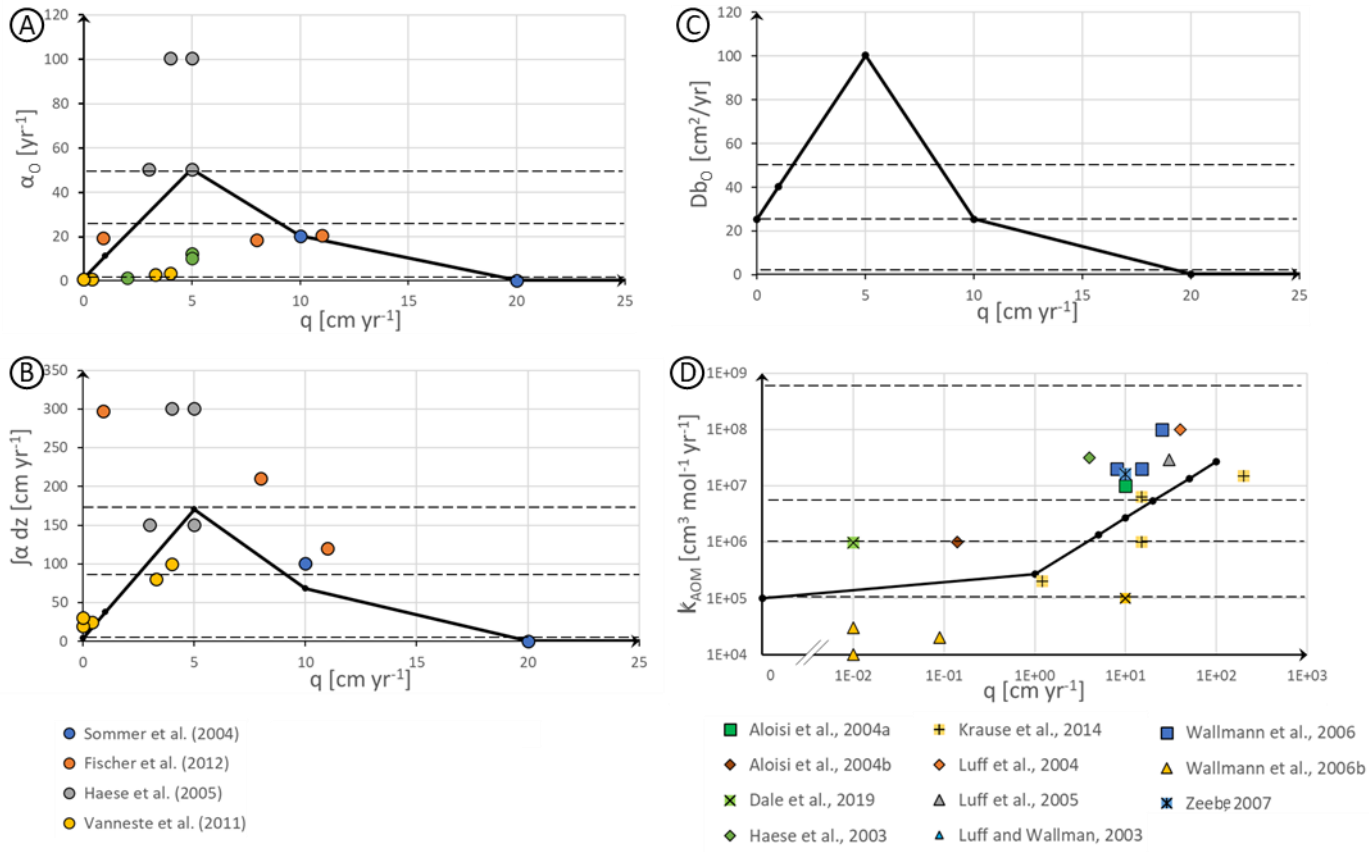

Figure 1: Parameter values as a function of fluid flow (q) for the baseline run compared to data reported in the literature: (a) bioirrigation coefficient at the sea floor (α0); (b) depth integrated bioirrigation rate over the modeled depth of bioirrigation (zirr); (c) bioturbation coefficient at the sea

floor (Db0) spanning the range reported by Solan et al. (2019); (c) kinetic rate constant for AOM (k_{AOM}). Solid lines represent model values for the baseline rune while horizontal dashed lines correspond to the values applied in the sensitivity analysis.

3. Results and discussion

3.1. Quantitative framework for analyzing the C-S system

The impact of each diagenetic reaction on pH is quantified using the approach of Jourabchi et al. (2005). In a nutshell, it assumes that any protolytic species of the carbonate and sulfide systems produced/consumed by a kinetically controlled reaction impacts the rate of change in pH. The influence of each reaction on pH is thus governed by the mass action laws (Table 1) and fulfills the condition of electric neutrality, leading to the following relationship:

$$\left(\frac{d[H^+]}{dt}\right)_i = \frac{t_a^i - (X_1 + 2X_2)t_c^i - S_1 t_s^i}{A_1} R^i \quad (8)$$

Where t_a^i, t_c^i and t_s^i are respectively the stoichiometric coefficients of the production or consumption of Ta, Tc and Ts by a given kinetic reaction i, with rate R^i, and where X1 and X2 are the relative contributions of HCO_3^- and CO_3^{2-} to Tc, respectively, and S1 is the relative contributions of HS^- to Ts:

$$HCO_3^- = X_1 Tc \quad (9)$$

$$CO_3^{2-} = X_2 Tc \quad (10)$$

$$HS^- = S_1 Ts \quad (11)$$

The denominator A_1, is given by Jourabchi et al. (2005):

$$A_1 = Tc\frac{\partial(X_1)}{\partial[H^+]} + 2Tc\frac{\partial(X_2)}{\partial[H^+]} + Ts\frac{\partial(S_1)}{\partial[H^+]} + Tb\frac{\partial\left({}^{Tb}/_{[B(OH)_4^-]}\right)}{\partial[H^+]} - \frac{[OH^-]}{[H^+]} - 1 \quad (12)$$

Because , in sea and porewaters, the total concentration of borate, Tb, is typically at least two orders of magnitude lower than that of total dissolved inorganic carbon, Tc, equation (12) can be simplified:

$$A_1 = Tc\frac{\partial(X_1)}{\partial[H^+]} + 2Tc\frac{\partial(X_2)}{\partial[H^+]} + Ts\frac{\partial(S_1)}{\partial[H^+]} - \frac{[OH^-]}{[H^+]} - 1 \quad (13)$$

A sign analysis of the individual terms in A_1 allows to qualitatively understand the role of each reaction in driving changes in pH:

- the ratio of hydroxyl and proton concentration is always positive,
- dS_1/dH^+ and dX_2/dH^+ are always negative,
- the sign of dX_1/dH^+ shifts from negative to positive with increasing pH (Fig 2A and B).

Within a typical range of pore water pH (i.e. 6.5-7.9) dX_2/dH^+ is almost equal to $-dX_1/dH^+$. Yet, because dX_2/dH^+ is multiplied by two (eq.13) and all other terms in A_1 are negative, the sign of A_1 is always negative (Fig 2C).

As a consequence, the sign of dH^+/dt, negative for proton consumption and positive for proton production, is determined solely by the sign of the numerator in equation 8. For instance, a reaction producing alkalinity, Ta (i.e. with a positive stoichiometric coefficient t_a), will have the tendency to consume protons (since A_1 is negative) and increase pH, while a reaction producing dissolved inorganic carbon, Tc, or sulfides, Ts, will have the opposite effect. However, many reactions influence Ta, as well as Tc and/or Ts and the net effect on pH will thus depend on the respective values of the stoichiometric coefficients, ta, tc and ts. Furthermore, the change in proton concentration also depends on the in-situ pH itself via the positive terms X_1, X_2 and S_1. As a result, a reaction with a given stoichiometry in terms of ta, tc and ts can result in both a decrease or increase in H^+ concentration depending on the ambient pH. In other words, the contribution of a given reaction to a change in pH depends on the ambient pH.

For instance, for AOM, ta, tc and ts, are respectively equal to +2, +1, +1 (Table 1), and since X_1+2X_2 and S1 are always less than 1 over the range of pH of interest, the ta term dominates the nominator in eq. 8 and AOM thus always consumes protons and increases pH within the range of environmental conditions encountered in marine sediments (Fig. 3). Furthermore, because the magnitude of X_1+2X_2 and S_1 increases with pH (Fig. 2), the consumption of protons by AOM becomes less efficient with increasing pH (Fig.3). Similarly, calcite dissolution (ta=+2, tc=+1, ts = 0) and precipitation (ta= -2; tc= -1; ts = 0) respectively consume and produce protons at any pH. For sulfate-reduction ta, tc and ts are respectively equal to +1.15, +1, +0.5 and, within the pH range of marine sediments, the difference between the first term and the last two terms on the right-hand side of the nominator of eq. 8 is thus smaller than for AOM. Since both X_1+2X_2 and S1 increase with pH, the effect of sulfate reduction on pH thus switches from consuming protons at low pH (up to about 6.9) to producing protons at high pH (Fig. 3).

Although the sign of dH^+/dt is solely controlled by the numerator of equation 8, the denominator, A1, influences the absolute magnitude of the rate of proton production/consumption. As A1 depends on Tc and Ts (equation 13), the change in proton concentration caused by a given reaction, taking place at a given pH, is inversely related to Tc and Ts of the solution. As such, the rate of change in proton concentration caused by a given rate of reaction is more important in seawater, with low Tc and Ts (Fig. 3A), than in the Tc and Ts charged connate fluid investigated here (Fig. 3C) or in a typical pore fluid at the SMTZ (Fig. 3B). In summary, while the sign of dH^+/dt is solely determined by the stoichiometries of the reactions, as well as ambient pH, the magnitude of dH^+/dt also depends on the fluid composition through Tc and Ts.

Following Jourabchi et al. (2005), the contribution of a reaction to the saturation state with respect to calcite Ω_{Cal} (equation 14) can be expressed as a function of their contribution to the production or consumption of calcium and carbonate ions, expressing the latter as a function of the previously derived rate of change in proton concentrations (equation 15).

$$\left(\frac{d\Omega_{Cal}}{dt}\right)_i = \frac{1}{K^*_{spCal}}\left[[CO_3^{2-}]\left(\frac{dCa^{2+}}{dt}\right)_i + [Ca^{2+}]\left(\frac{dCO_3^{2-}}{dt}\right)_i\right] \quad (14)$$

$$\left(\frac{d\Omega_{Cal}}{dt}\right)_i = \frac{1}{K^*_{spCal}}\left[[CO_3^{2-}]\left(\frac{dCa^{2+}}{dt}\right)_i + [Ca^{2+}]\left(\underbrace{t_c^i X_2 R^i}_{\text{term 1}} + \underbrace{Tc\frac{\partial X_2}{\partial [H^+]}\left(\frac{d[H^+]}{dt}\right)_i}_{\text{term 2}}\right)\right] \quad (15)$$

where term 1 and term 2 result from applying the chain rule of derivation to eq. (10). In the reaction network implemented here, solely the precipitation and dissolution of calcite affect the concentration of calcium ions and, as such, $dCa^{2+}/dt=0$ for all other reactions. The sign of term 1 merely depends on the sign of t_c^i, as X_2 and R^i are all defined as positive. The sign of term 2 depends on the sign of dH^+/dt, as Tc is always positive and dX_2/dH^+ is always negative. Thus, for reactions like AOM or sulfate-reduction that produce dissolved inorganic carbon, Tc, term 1 is always positive. Term 2 is also always positive for AOM ($dH^+/dt < 0$) yet, for sulfate reduction, term 2 changes from positive to negative with an increase in pH. This shift in sign for $d\Omega_{Cal}/dt$ occurs at a different pH than the shift in sign for dH^+/dt, because it also depends on the values of X_2 and dX_2/dH^+. Furthermore and in contrast to the rate of change in proton concentration, the pH value of the shift in sign of $d\Omega_{Cal}/dt$ is also a function of the Tc term or, in other words, the pattern of change in $d\Omega_{Cal}/dt$ as a function of pH slightly differs between seawater, connate fluid or a typical pore fluid at the SMTZ (Fig. 3D, E, F).

Overall, our theoretical framework reveals that over the pH range that is commonly observed in porewaters (6.5-7.9), AOM always promotes calcite saturation. This effect is especially pronounced under high ambient pH. In contrast, sulfate reduction promotes calcite precipitation at low pH values and calcite dissolution at high pH values. The shift between these regimes happens at pH values between 7 and 7.1 depending on fluid composition (Fig. 3. D, E, F). Calcite precipitation and dissolution respectively consume (negative dCa^{2+}/dt) and produce calcium ions (positive dCa^{2+}/dt), which, in addition to their effects on terms 1 and 2, induces a negative feedback on the reactions themselves. In other words, precipitation/dissolution respectively decrease/increase the saturation state with respect to calcite.

The concentrations of Tc and Ts impact $d\Omega_{Cal}/dt$ solely via term 2; both directly via the ascribed Tc coefficient and indirectly via dH^+/dt. Within the compositional range of the studied fluids (sea water and connate fluid), variations of Tc and Ts are nearly inversely proportional to variations

of dH^+/dt (see above). As a consequence, the order of magnitude of term 2 remains constant and the concentration of Tc and Ts in the fluid thus does not exert a major influence on the absolute magnitude of $d\Omega_{Cal}/dt$ (Fig 3. C, D, E). In summary, our theoretical analysis reveals that over the range of investigated pH (6.5-7.9) and independent on the exact fluid composition, AOM always consumes protons and produces Ω_{Cal} at significantly larger rates than sulfate-reduction. Therefore, per unit rate, AOM is always more powerful than sulfate-reduction in promoting the precipitation of authigenic carbonates.

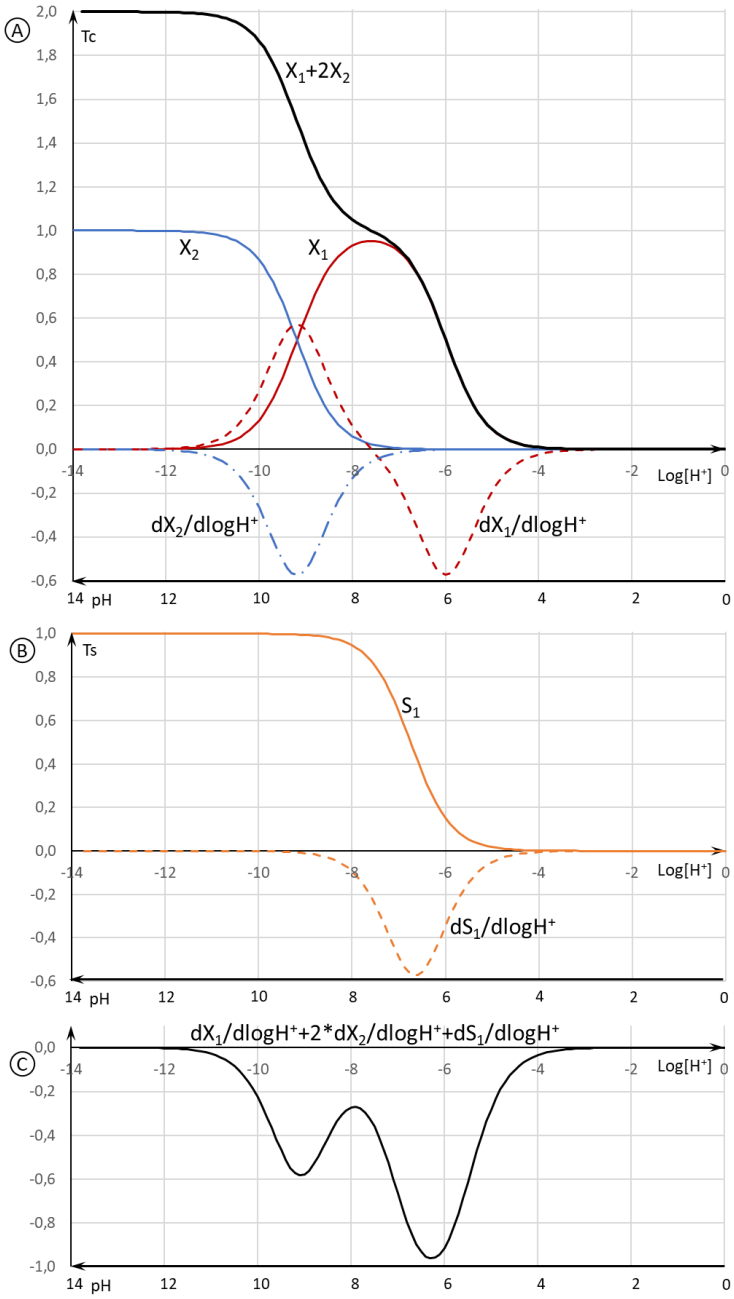

Figure 2. A) Proportions of HCO_3^- and CO_3^{2-} to the total dissolved carbonate concentration (Tc), respectively noted X_1 and X_2, and distribution of X_1+2X_2, $dX_1/dlogH^+$ and $dX_2/dlogH^+$ as a function of pH; B) Proportion of HS^-, noted S1, to the total dissolved sulfide concentration (Ts), and distribution of $dS_1/dlogH^+$ as a function of pH, C) Distribution of $dX_1/dlogH^+ + 2dX_2/dlogH^+ + dS_1/dlogH^+$ as a function of pH. See text for further details. All graphs are given at the temperature and pressure of the baseline model (10°C; 20 bar).

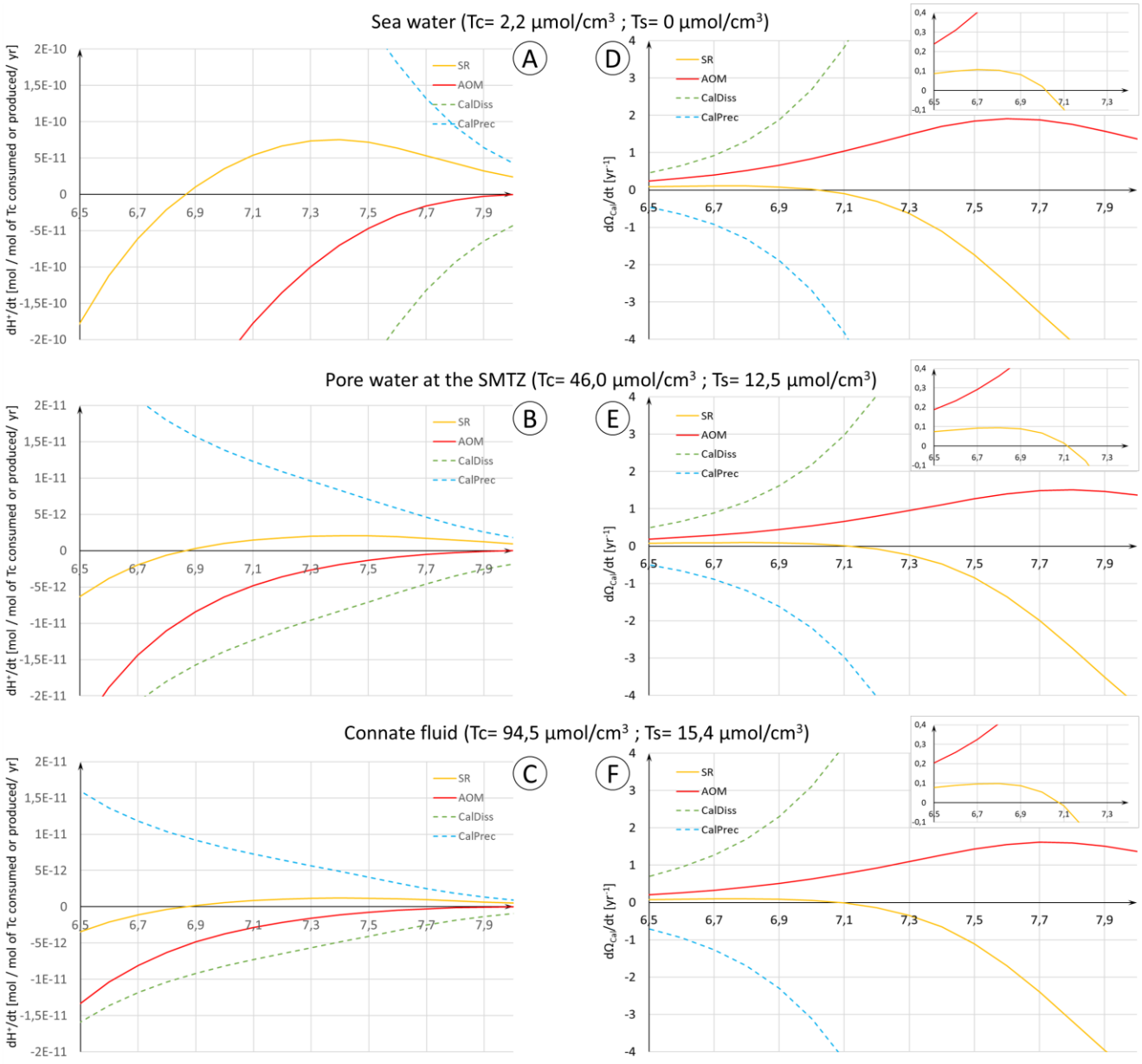

Figure 3. Rate of change in proton concentration and associated rate of change in Ω_{Cal}, at the temperature and pressure of the baseline model (10°C; 20 bar), as a function of the pH for solutions of different total dissolved inorganic carbonate (Tc) and total dissolved sulfide (Ts), concentrations corresponding to sea water (A, D), to pore water at the depth of maximal rate of AOM (14 cm) in the baseline model (q=10 cm/yr) (B, E), and to the connate fluid (C, F). Curves are shown for the reactions of sulfate reduction (SR), anaerobic oxidation of CH_4 (AOM), calcite dissolution (CalDiss) and calcite precipitation (CalPrec). Note that the scale of A) is ten times larger than in B) and C). The inset in D), E) and F) zoom in the area of the diagrams where sulfate-reduction switches from production to consumption of Ω_{Cal}. The rates of change in H^+ and Ω_{Cal} are plotted for reaction rates of SR and AOM set arbitrarily to 1 µmol SO_4^{2-} consumed cm^{-3} yr^{-1} (which, according to the stoichiometry

of the reactions, is equivalent to 1 µmol Tc produced $cm^{-3}\,yr^{-1}$, see Table 1), and for carbonate precipitation/dissolution set to 1 µmol of Tc consumed/produced $cm^{-3}\,yr^{-1}$.

3.2. Environmental drivers of the coupled AOM-carbonate dynamics

3.2.1. Baseline simulation for passive and active settings

Figure 4 illustrates the simulated baseline, steady-state depth profiles of concentrations, reaction rates, as well as of the rate of change in pH (dH^+/dt) and carbonate saturation state ($d\Omega_{Cal}/dt$) for both a passive (q = 0 cm y^{-1}) and an active (q = 10 cm y^{-1}) setting. It shows that the presence of fluid flow exerts an important influence on depth profiles, as well as on the total amount of seep carbonate precipitated and its dominant controls.

In the passive setting (Fig 4I), SR, as well as AOM that is driven by the diffusive transport of biogenically produced CH_4 in deep sediments, completely deplete porewater sulfate at 160 cm depth (Fig. 4Ia). SR rate is high in the shallow sediment but rapidly decrease with depth due to the decrease in POC reactivity with age, as shown by eq. 5 (Fig. 4Ig). Due to the relatively low AOM efficiency that has been assumed for the baseline scenario ($k_{AOM=}\,10^5\ cm^3\ mol^{-1}\ yr^{-1}$), sulfate and CH_4 coexist over a depth interval of about 50 cm around the SMTZ. Below the SMTZ, methanogenesis dominates POC degradation, but the rate remains low due to the continuous decrease in POC reactivity. Both SR and methanogenesis generate significant amounts of Tc and Ta (mostly bicarbonate alkalinity), while SR also produces large quantities of Ts in the porewaters (Figs. 4Id, 4Ie). SR exerts the dominant control on the acid-base equilibriums in the upper portion of the sediment column (<50 cm). Due to the comparably high ambient pH, it generates protons ($dH^+/dt > 0$), and do so at a relatively high rate due to the low pore water Tc and Ts concentrations (see Fig. 3A for a surrogate of such behavior). As a consequence, the porewater pH rapidly decreases with depth, shifting the carbonate equilibriums towards H_2CO_3 and, thus driving calcite dissolution. However, because of the decrease in pH with depth, SR subsequently switches from a proton generating process to a proton consuming process at about 20 cm within the sediment (Fig 4Ih). The resulting stabilization of ambient pH and the increasing accumulation of Tc increase the saturation state of porewaters and calcite precipitation is simulated by SR down to a sediment depth of about 80 cm (Fig. 4Ii). Within this zone, the progressive decrease in SR with depth is compensated by the rise of AOM, consuming proton, and progressively becoming the dominant control on the acid-base equilibriums (methanogenesis exerts an insignificant contribution on the pH-carbonate dynamics). The concurrent proton production by calcite precipitation acts as an effective negative feedback against the pH increase triggered by AOM (Fig 4Ih). Fig 4Ib shows that the dissolution of sedimentary calcite in the shallow dissolution zone is largely compensated by the precipitation of authigenic calcite in the lower portion of the core. Interestingly, we note that calcite dissolution is simulated over a wider depth interval than the one

delineated by the SR driven decrease in saturation state ($d\Omega_{Cal}/dt<0$) and even proceeds into sediment depths where both SR and AOM act to increase Ω_{Cal} ($d\Omega_{Cal}/dt>0$). These simulation results highlight that, in addition to biogeochemical processes, differential transport of Tc, Ta and Ts through diffusion and biological mixing can also exert an important control on pH and saturation state dynamics in marine sediments. Transport processes effectively blur the limits between the different reaction zones, and their effect on pH and saturation state explains why calcite dissolution can occur at sediment depths where all biogeochemical reactions act to increase the saturation state ($d\Omega_{Cal}/dt > 0$).

With active fluid flow, the simulated AOM rate is about 5 times larger than the maximum rate of SR, and about 50 times larger than the maximum AOM rate simulated for the passive setting (Fig.4II). As a consequence, the penetration depth of sulfate shifts upcore and the depth interval at which sulfate and CH_4 coexist is reduced (Fig4IIa). In addition, the more efficient upward migration of pore fluids enriched in Tc, Ta and Ts also increases the concentration of these chemical species in the core. The decrease of pH below the sea floor is slightly sharper than in the passive case, due to the production of protons by SR on the one side, similarly to the passive case, and to the upward advection of acidic fluids from below on the other side (Tc/Ta ratio at 30 cm of about 1.2 (Figs. 4IIe,f compared to a ratio close to 1 in the passive case Figs. 4Ie,f). However, similar to the passive case, the pH profile tends to stabilize at a near constant value within the SMTZ. Here, the influence of AOM and calcite precipitation on the pH partly compensate, as illustrated by a set of models with either the AOM or calcite precipitation rates arbitrary set to 0 (Fig 4IIc). While the absence of AOM results in a larger drop in pH, deactivating calcite precipitation increases pH. In terms of calcite dynamics, similar to the passive case, dissolution is induced by SR in the uppermost portion of the sediment core but at greater depths SR exerts a negligible influence on calcite precipitation due to the dominance of AOM. Interestingly, due the negative effect of decreasing pH on $d\Omega_{Cal}/dt$ induced by AOM (Fig. 3E), the highest rate of calcite precipitation is located slightly above the depth at which maximum AOM rate are simulated (Fig. 4IIg). In addition, total calcite precipitation is much larger than total calcite dissolution due to the reduced residence times in the dissolution zone. Bioturbation, simulated here as a diffusive process, results in significantly shorter residence times of solid sediment at shallow depth, where dissolution is active, compared to sediment located at greater depth, where solely burial and compaction act on solid advection downward. As a consequence, the time available for precipitation is in this case much longer than for dissolution and a pronounced increase in the overall amount of calcite is simulated with depth (Fig. 4IIb). This contrasts with the passive case where a significant fraction of the dissolution occurs below the bioturbated layer, at depths where the residence time is comparable to that in the precipitation zone.

In summary, active fluid flow considerably increases the amount of authigenic carbonate that precipitates below the mixed layer of the sediment. It supports intense AOM rates that in turn become the dominant driver of carbonate precipitation. At the same time, fluid flow pushes the SMTZ to shallower sediment depth and thus constrains SR to the bioturbated zone of the sediment where its quantitative impact on the amount of carbonate that can dissolve or form is limited due to the short timescale for reaction. In contrast, the net amount of carbonate precipitated at the bottom of the sediment core in the passive setting depends on both AOM and SR, the latter process triggering both calcite dissolution and precipitation.

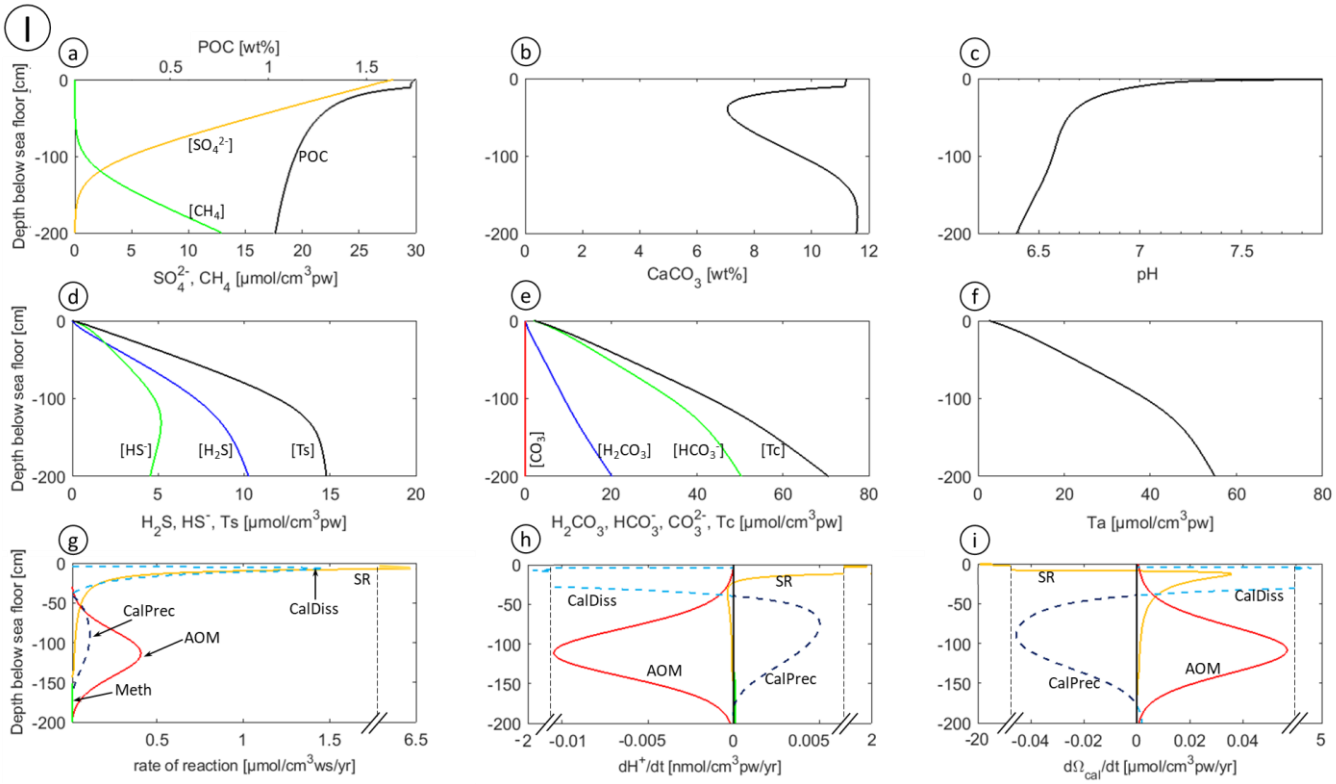

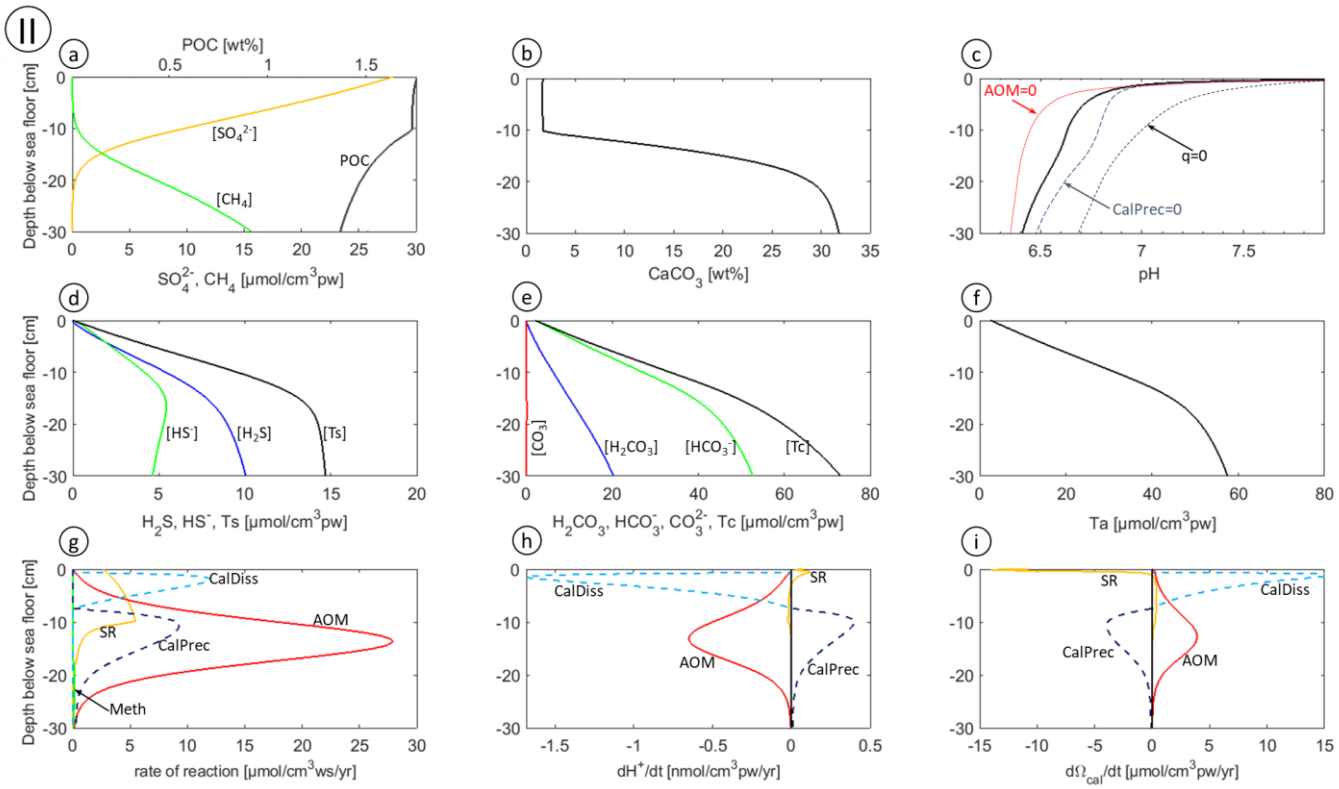

Figure 4: Model profiles for the baseline run (sedimentation rate w = 0.1 cm yr^{-1}; temperature= 10°C; water depth = 200 m); I) with q= 0 cm/yr; II) with q=10 cm/yr. a) POC, SO_4^{2-} and CH_4, b) $CaCO_3$, c) pH, d) HS^-, H_2S and Ts; e) CO_3^{2-}, HCO_3^-, H_2CO_3 and Tc; f) Ta; g) rates of reactions for organoclastic sulfate reduction (SR), methanogenesis (Meth), anaerobic oxidation of CH_4 (AOM), calcite dissolution (CalDiss), and precipitation (CalPrec); h) Contribution of each of these reactions to dH^+/dt and; h) to $d\Omega_{Cal}/dt$. In panel IIc, the pH profile is also reproduced for q= 0, and simulated for AOM and CalPrec rates set to 0, respectively. Note that bioturbation efficiently homogenizes the POC concentration in the bioturbated layer (first 10 cm), implying that SR (expressed in mol/cm^3 of POC/yr) remains almost constant within this interval. The apparent increase of SR with depth in the bioturbated layer, expressed in mol/cm^3ws /yr, is due to the sharp decrease of porosity at shallow depth. cm^3ws stands for cubic centimeters of wet sediment (i.e. the solid sedimentary participles plus the pore water), cm^3pw stands for cubic centimeters of pore water, and wt% stands for weight per cent.

3.2.2. Control of fluid flow on carbonate precipitation

Figure 5 provides further insights into the effect of fluid flow on authigenic carbonate precipitation and its underling mechanisms. It shows depth profiles of calcite precipitation/dissolution rates over a large range of plausible fluid flow velocities, q. Model results reveal that the maximum rate of precipitation increases with q, from 0.02 µmol cm^{-3} y^{-1} at q=0 cm y^{-1} to 160 µmol cm^{-3} y^{-1} at q=100 cm y^{-1}. Meanwhile, the depth at which the maximum precipitation rate

occurs moves upcore from about 115 cm under no flow conditions (no shown) to only a few cms for q=100 cm y^{-1} and the thickness of the precipitation zone decreases. In the presence of active fluid flow, dissolution rates are generally constrained to the shallowest, often bioturbated sediment layers (note that Db is set to 0 for q≥ 20 cm yr^{-1}) and follow the same trend as precipitation with increasing q. Therefore, and as already highlighted in the above section, dissolution exerts a minor effect on the amount of calcite compared to precipitation and further decreases as q increases.

Table 7 summarizes simulated depth-integrated rates for the baseline model (water depth = 200 m) and for the baseline model assuming a water depth of 1000 m. The two model set-ups facilitate a direct comparison with previously published depth-integrated rates, as well as rates of growth of concretions across a range of coastal and slope environments (see further discussion in section 5.1). While depth integrated rates frequently reported in the literature are often implicitly interpreted as a quantitative measure for the production or consumption of porewater species via reactions, making the implicit assumption that the rate of burial is linearly correlated to the sediment depth, the translation of burial depth to burial time (and ultimately residence time) is however more complex. This is due to the effect of compaction, and most importantly to the effect of mixing by bioturbation (Fig 5). Nevertheless, depth-integrated rates of AOM are of the same order of magnitude than previously published rates inferred from observational data and collated by Regnier et al. (2011) for similar water depths and range of fluid flow velocities, thus confirming that our theoretical model framework represents indeed realistic conditions. In addition, results confirm that AOM and SR rates are roughly equal for a passive setting but AOM rates are three times higher at q = 5 cm y^{-1} and 10 times higher at q = 20 cm yr^{-1} (water depth = 200m). Thus, in active settings characterized by high fluid flow velocities (q>10 cm yr^{-1}), AOM exerts the dominant control on calcite precipitation because it proceeds at higher rates, while under low to moderate fluid flow conditions (q<10 cm yr^{-1}) AOM also exerts the dominant control on calcite precipitation because SR is constrained to the bioturbated layer, characterized by short-residence times. The patterns identified in our baseline runs (section 3.2.1) are thus also valid over the range of fluid flow conditions and water depths investigated here.

Interestingly, the ratio between the depth integrated rate of AOM and the depth integrated rate of calcite precipitation is larger than one and remains relatively constant with an increase in q (3.3 – 4 at 200 m water depth and 4.4 -5.2 at 1000 m water depth). Given that the stoichiometric coefficient for Tc production by AOM and Tc consumption by calcite precipitation are both 1, a ratio > 1 indicates that a large fraction of the DIC produced by AOM is not converted into seep carbonates, but, instead, bypass the SMTZ and leaks trough the sea floor. Model results thus allow deriving a first-order estimate of the CH_4-$CaCO_3$ conversion factor, 1/3-1/5 of the depth-integrated AOM rate depending on the specific environmental conditions, similarly as calculated by Akam et al., (2020) at

global scale. The ratio of the depth integrated AOM rate to net calcite precipitated (production – dissolution) is significantly larger than the ratio to calcite precipitation and decreases with q (from 12 to about 3 at 200 m water depth). In addition, model results show that the efficiency of the AOM barrier in consuming the upward migrating CH_4 is not always 100%. Although the ratio between integrated AOM rates and the CH_4 flux through the lower boundary of our model remains close to 1 at low-moderate q, it drops sharply to 0.3-0.4 for very high fluid flow velocities (i.e. q = 100 cm yr^{-1}). This is in agreement with previously published simulation results showing that enhanced advective flux facilitates the escape of dissolved CH_4 fluxes through the sediment-water interface (Pugglini et al., 2020). As a consequence, integrated AOM and calcite precipitation rates scale nearly linearly with fluid flow between q=5-10 cm yr^{-1}, but increase slower under more intense fluid flow conditions (Table 7). For instance, between 20 and 100 cm $yr^{-1,}$ calcite precipitation increases by about a factor of 2 for a 5-fold increase in q. Despite CH_4 and Tc loss at high flow rate, carbonate precipitation still increases over the full range of q investigated here. These findings are in contrast to the modeling results of Luff et al. (2004) that predict a suppression of carbonate precipitation under high fluid flow velocities (q> 80 cm/yr) at Hydrate Ridge (off Oregon). Karaca et al. (2010) also simulated a reduced rate of carbonate precipitation for q= 200 cm yr^{-1}, based on pore water profiles collected at an active mud volcano in the accretionary prism offshore Costa Rica (Schmidt et al., 2005; Linke et al., 2005; Moerz et al.,2005). The discrepancies between the simulated behavior can be explained by differences in the efficiency of the AOM. Luff et al. (2004) observes a large CH_4 escape through the sediment-water interface at high q. This escape is a direct consequence of a constant k_{AOM} value applied across the full range of fluid flows velocities, resulting in a lower AOM efficiency than in our scenarios, that, in agreement with observations (e.g. Regnier et al, 2011), applies increasing k_{AOM} values with an increase q. Similarly, Karaca et al. (2010) also selected a surprisingly low k_{AOM} value that is comparable to their selected value for passive settings. Indeed, such low k_{AOM} values are characteristic for a low biomass of the resident AOM community. Sediment cores might have been taken soon after an eruption of CH_4, at a time that was sufficient to allow pore water concentration profiles to adjust to the new conditions (monthly time scale; Taylor et al., 2015; Van de Velde et al., 2018), but insufficient for the microbial AOM biomass to increase the AOM efficiency (i.e. k_{AOM} value) accordingly (decadal time scale; Dale et al., 2006, 2008; Nauhaus et al., 2007; Puglini et al., 2020).

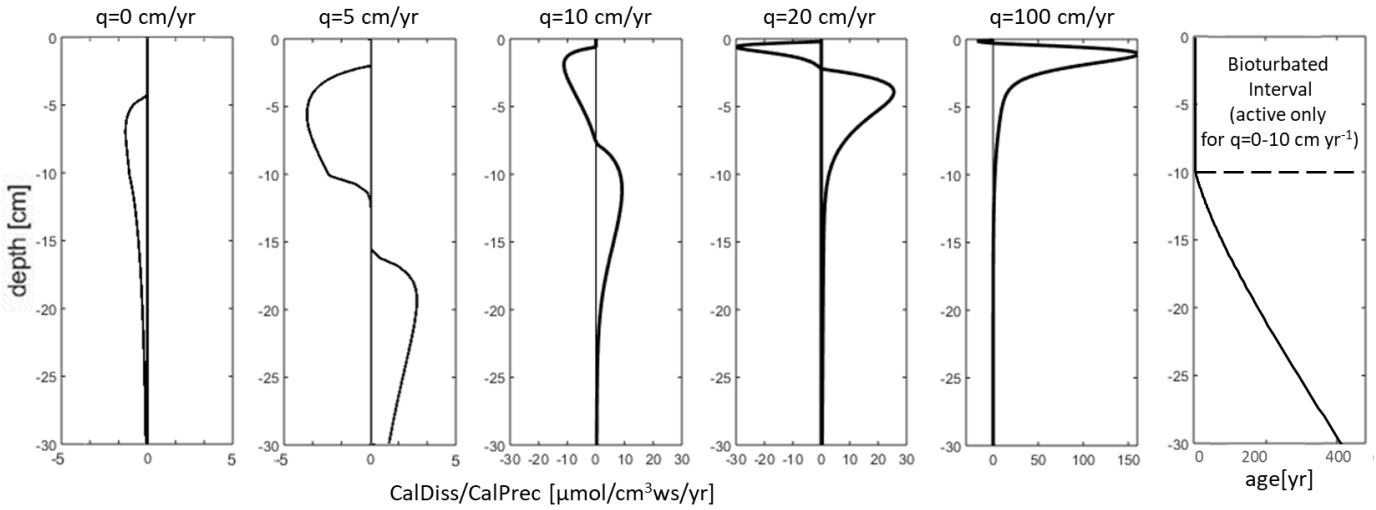

Figure 5: depth profiles of calcite dissolution (CalDiss) / precipitation rates (CalPrec) for a range of fluid flow values (q) at the temperature and pressure of the baseline model (sedimentation rate w = 0.1 cm yr^{-1}; temperature= 10°C; water depth = 200 m). Dissolution and precipitation rates are reported as negative and positive numbers, respectively. Note the different scales for the x-axes. The panel on the right hand side shows the age of each sediment layer for w = 0.1 cm yr^{-1}, assuming that the age in the bioturbated interval is homogeneous and much shorter than below, where only burial and compaction is active. cm^3ws stands for cubic centimeters of wet sediment.

	baseline model at 200 m water depth ∫rate dz [µmol cm-2ws yr-1]				
reaction	q=0 cm/yr	q=5 cm/yr	q=10 cm/yr	q=20 cm/yr	q=100 cm/yr
SR	49	45	42	48	25
AOM	30	144	286	494	1.151
CalDiss	17	30	44	26	3
CalPrec	9	42	84	124	326
net CalPrec	-7	12	41	98	323
AOM/SR	0,6	3,2	6,8	10,2	46,6
AOM/CalPrec	3,3	3,5	3,4	4,0	3,5
AOM/NetCalPrec	-4,0	12,5	7,0	5,1	3,6
AOM/Advected CH4	-	1,0	1,0	0,9	0,4
$CaCO_3$ crust growth rate [cm/kyr]	0,4	1,8	3,6	5,3	13,9
advected FCH_4 [mol/cm^2_{ws}/yr]	0	142	283	566	2.830

	baseline model at 1000 m water depth ∫rate dz [µmol cm-2ws yr-1]				
reaction	q=0 cm/yr	q=5 cm/yr	q=10 cm/yr	q=20 cm/yr	q=100 cm/yr
SR	47	43	40	42	24
AOM	78	481	854	1194	2947
CalDiss	20	33	43	3	-
CalPrec	18	99	178	228	-
net CalPrec	-2	66	135	224	-
AOM/SR	1,7	11,3	21,4	28,4	121,3
AOM/CalPrec	4,4	4,9	4,8	5,2	-
AOM/NetCalPrec	0,0	7,3	6,3	5,3	-
AOM/Advected CH4	-	0,9	0,8	0,6	0,3
$CaCO_3$ crust growth rate [cm/kyr]	0,8	4,2	7,6	9,7	-
advected FCH_4 [mol/cm^2_{ws}/yr]	0	535	1070	2140	10700

Table 7: Depth integrated rates of organoclastic sulfate reduction (SR), anaerobic oxidation of CH4 (AOM), calcite dissolution (CalDiss), calcite precipitation (CalPrec), and net calcite precipitation (net CalPrec = CalPrec - CalDiss) for a range of fluid flow values (q) in the baseline model conditions (sedimentation rate w = 0.1 cm yr^{-1}; temperature= 10°C; water depth = 200 m). Values are also reported for a water depth of 1000 m. The advection rate of CH_4, FCH_4, is equal to the fluid flow (q) times the CH_4 saturation concentration. The growth rate of a carbonate concretion and key diagnostic ratios of the coupled CH_4-AOM-carbonate dynamics are also reported.

3.2.3. Quantitative relationship between fluid flow and carbonate precipitation

Model results (Fig.5) show that increasing fluid flow rates result in a nonlinear increase in maximum carbonate precipitation rates. However, at the same time, they also lead to a decrease in the width of the precipitation zone, thus, reducing the residence time of solid sediment in the precipitation zone. The quantitative relationship between fluid flow and integrated amount of carbonate precipitated (Fig. 6) shows that this opposing effects, an increase in maximum precipitation rates and a concomitant thinning of precipitation zones, result in an almost linear relationship between the amount of precipitated carbonate and fluid flow at low to intermediate q that then slightly levels off at high q values (q> 20 cm yr^{-1}) and ultimately leads to full cementation at

q≥ 38 cm yr^{-1} under the specific environmental conditions chosen for our baseline scenario (Fig 6). We can thus distinguish two different regimes in the FCH_4-$CaCO_3$ relationship: 1) a "quantitative" domain in which the flux of CH_4 can be directly estimated from the amount of authigenic calcite that is observed in the sediment, and 2) a "threshold" domain, characterized by full cementation, that merely provides a lower bound estimate of the CH4 flux, which corresponds to the lowest FCH_4 at which full cementation is attained. In addition, Table 7 shows that up to q = 20 cm yr^{-1}, most of the CH4 rising from below is oxidized by AOM (AOM/FCH_4 = 0.9) highlighting that the condition AOM/FCH_4≈1 is also fulfilled within the quantitative domain.

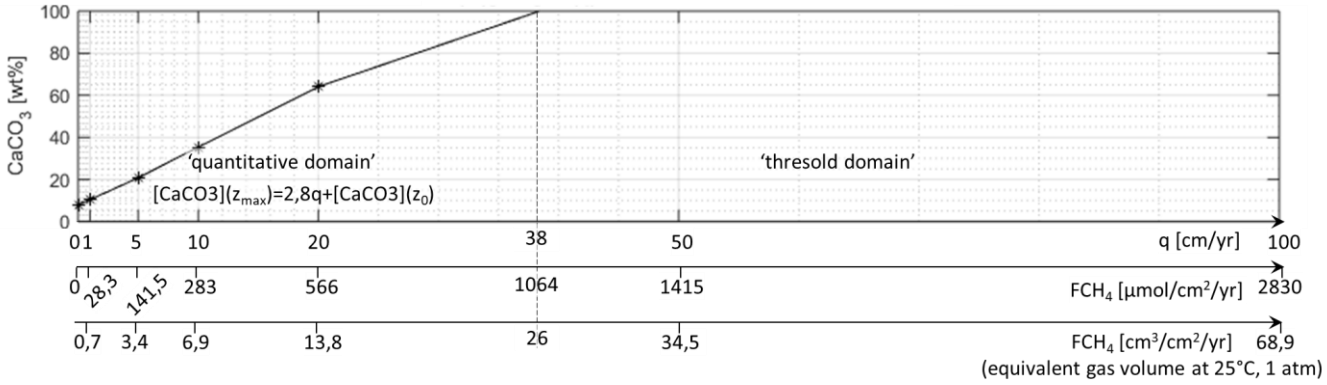

Figure 6: Amount of calcite at the bottom of the modeled core as a function of the fluid flow (q) and the flux of CH_4, FCH_4, for the baseline model (sedimentation rate w = 0.1 cm yr^{-1}; temperature= 10°C; water depth = 200 m). The amount of calcite is almost linearly correlated to fluid flow at low q values, and reaches full cementation from q= 38 cm yr^{-1}. The volume flux of gas equivalent to the flux of dissolved CH_4 is provided at standard temperature and pressure (25°C; 1 atm), conventionally used in petroleum geology.

3.3. Seep carbonates as quantitative proxies for active CH_4 flux

In the previous section, we derived a quantitative relationship between active CH_4 flux and the amount of carbonate that precipitates in the sediment under a unique set of environmental conditions, as well as at the specific water depth and sedimentation rate chosen for the baseline simulation. Here, we extend the scope of the F_{CH4}-$CaCO_3$ relationships over a broad range of different water depths and sedimentation rates. In addition, the baseline simulation described in the previous section uses kinetic rate constants of AOM (k_{AOM}) and bioturbation/bioirrigation parameters that are a function of the upward fluid velocity, q. Functional dependencies were derived from a compilation of observational data (Fig 1), but are entailed with a certain degree of uncertainty. Therefore, we also test the sensitivity of F_{CH4}-$CaCO_3$ relationships to different bioturbation (Db) and bioirrigation (bioirr)

intensity as well as k_{AOM} values that span the entire range of values previously reported in the literature.

3.3.1. F_{CH4}-$CaCO_3$ relationships as a function of water depth and sedimentation rates

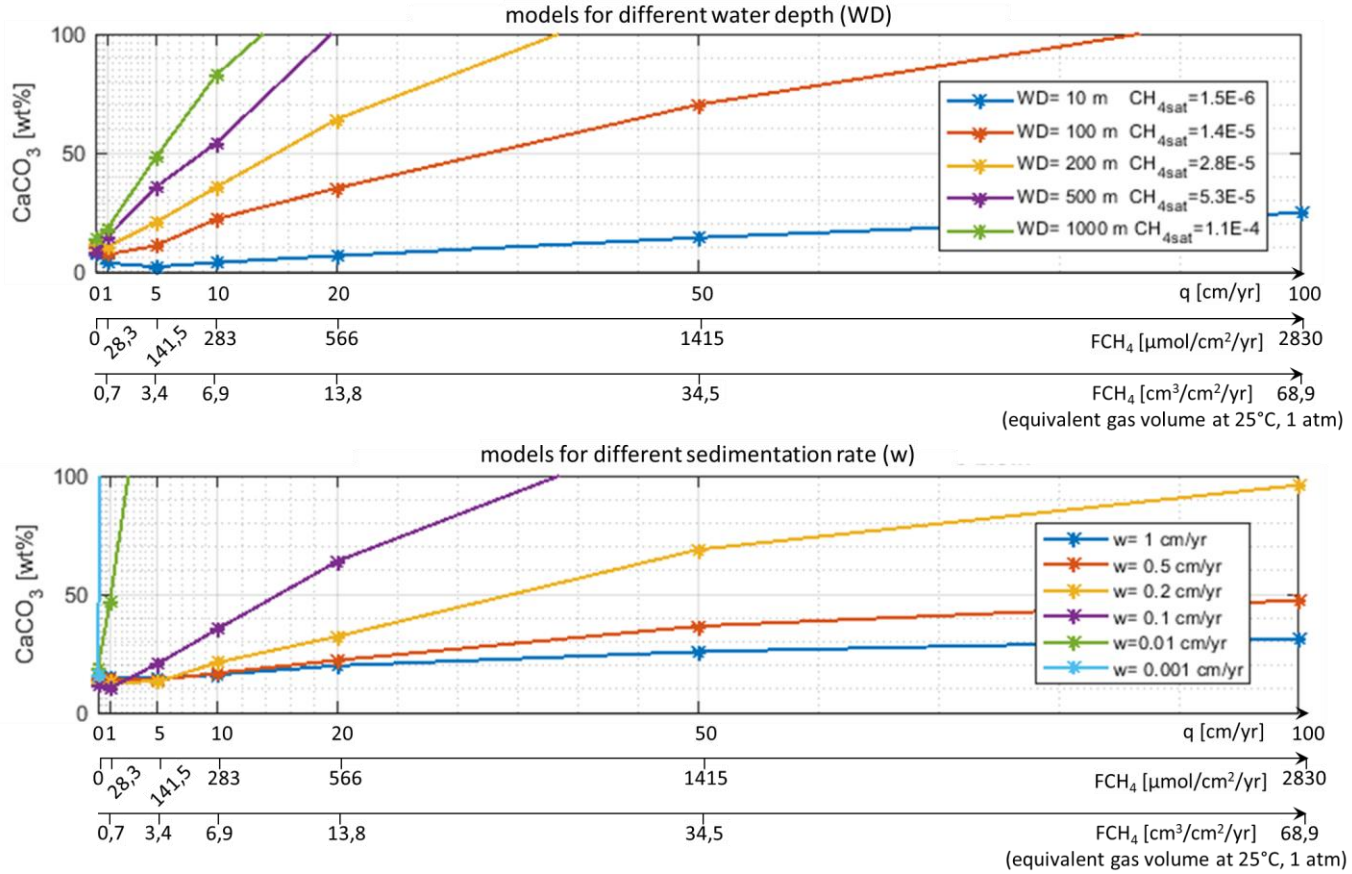

Figure 7: Amount of calcite at the bottom of the modeled core as a function of the fluid flow (q) and the flux of CH_4 (FCH_4) for A) several water depth, and B) several sedimentation rate.

Model results show that changes in water depths or sedimentation exert an important influence on the switch between the quantitative and a threshold domain of the F_{CH4}-$CaCO_3$ relationships. Variations in water depth induce a considerable increase in FCH_4 for any given fluid advection value (q) due to the nearly proportional increase in the equilibrium concentration of dissolved CH_4 (CH_{4sat}) with increasing hydrostatic pressure (at the given T and S assigned in the model; Table 6). As a result, full cementation occurs at lower q values for deeper water depths. For instance, the quantitative regime is restricted to about 10-20 cm yr^{-1} for a water depth of 1000 m, while it extends beyond 100 cm yr^{-1} for a water depth of 10 m. In addition, for a water depth equal to 1000 m, at q values as low as 5-10 cm yr^{-1}, a significant fraction of the CH_4 flux escapes through the sediment-water interface (Table 7), thus further restricting the quantitative regime. Another

interesting feature is the increase in the ratio of integrated AOM to calcite precipitation rates with increasing water depth (Table 7). This finding highlights that, in addition to the effect of water depth on CH_4 solubility, water depth also exerts an important influence on the solubility of calcite through the pressure effects on the apparent equilibrium constant (K^*_{spCal}). As water depth increases, the saturation state of porewaters with respect to calcite decreases. Such thermodynamic control reduces the width of the precipitation zone, but this effect is nevertheless of second order as oversaturation and thus the precipitation zone are mainly controlled by AOM and, thus, the water depth-dependent CH_4 fluxes from below.

The FCH_4-$CaCO_3$ relationship is also strongly sensitive to the sedimentation rate, w. For instance, at a water depth of 200 m, increasing w by a factor of 2 (from 0.1 to 0.2 cm yr^{-1}) extends the quantitative domain to the entire range of fluid flow investigated here. However, as sedimentation rate increases further (e.g. w= 1 cm yr^{-1}), the short residence time in the SMTZ results in overall low amounts of calcite precipitated and a weak sensitivity to the fluid flow rate. In contrast, for low sedimentation rates (w< 0,01 cm yr^{-1}), long residence times in the SMTZ lead to full cementation as soon as fluid flow exceeds 1 cm yr^{-1}, limiting again the quantitative domain. Residence time is here the first-order control on the amount of carbonate precipitated, but is not the only one as reaction rates and diffusive transport (both influencing dΩ/dt) are also affected by the burial rate.

Overall, our results highlight that the use of seep carbonates as quantitative proxies for fluid flow is powerful for shelf settings, but limited for greater water depths. There, its applicability is optimal for a range of sedimentation rate roughly comprised between 0.05 and 1 cm yr^{-1}. At lower sedimentation rates (<0.01 cm yr^{-1}) full cementation occurs and only a lower bound estimate can be provided, while at high sedimentation rates (>1 cm yr^{-1}) the amount of $CaCO_3$ cannot be used as a quantitative proxy of FCH_4 anymore.

3.3.2 Sensitivity of the F_{CH4}-$CaCO_3$ relationships to poorly constrained parameters

Sensitivity to kaom

To assess the sensitivity of our model results to uncertainties in the value of k_{AOM}, we here explore four different scenarios: a low k_{AOM} value typical of passive settings (1*10^5 cm^3/mol/yr), a typical value for an active setting (5*10^6 cm^3/mol/yr); an extremely high value (5*10^8 cm^3/mol/yr,) and an intermediate value (1*10^6 cm^3/mol/yr, Regnier et al., 2011).

Model results show that for the lowest and intermediate k_{AOM} values, the amount of calcite stays almost constant with an increase in q (Fig. 8a). Merely, a very weak linear increase is simulated

until q= 10 cm yr^{-1} where it reaches a plateau. Results thus indicate that, in these scenarios, the rate of precipitation is kinetically limited by the rate of AOM. As a consequence, a fraction of the CH4 flux by-passes the SMTZ and escapes through the sea floor. For the two k_{AOM} values corresponding to active settings, the increase in the amount of calcite with an increase in q is almost identically until q= 20 cm yr^{-1}, because in this fluid flow range the AOM rate is mainly controlled by the availability of CH4. These k_{AOM} values provide an AOM capacity that is able to entirely consume the CH_4 fluxes in the SMTZ (see table 7: AOM/FCH_4= 0.9 at q= 20 cm yr^{-1} for k_{AOM} = 5*10^6 cm^3/mol/yr at 200 m water depth). At higher q, full cementation is simulated for both k_{AOM} values.

Our model results thus indicate that although the exact value of k_{AOM} in active setting is associated with a high uncertainty, up to two-order of magnitude variations of k_{AOM} do not significantly impact the results. However, they also indicate that unusually low k_{AOM} values compromise the use of seep carbonates as proxies for CH_4 flow. Nevertheless, such low k_{AOM} values are unrealistic for active fluid flow regimes, where a large and efficient AOM community develops at steady state (Fig. 1, D) (Pugligni et al., 2020; Regnier et al., 2011). Yet, low k_{AOM} have been observed in active settings under transient conditions, due to the delayed growth response of the resident microbial AOM community to perturbations. It has been shown that a significant fraction of the CH_4 flux can bypass the SMTZ over a decadal time scale due to the time lag necessary for the growth of the microbial population (Nauhaus et al., 2007; Dale et al., 2008). Thus, a short release of CH_4 would not be recorded by authigenic carbonate precipitation. Conversely, CH4 would rise up to the oxic zone of the sediment, where aerobic oxidation of CH_4 may promote carbonate dissolution, such as suggested based on petrographic observations by Blouet et al. (2017).

Sensitivity to Db

Model results reveal that the FCH_4-$CaCO_3$ relationship is slightly sensitive to the presence of bioturbating organisms, and almost insensitive to the intensity of the bioturbation (i.e. Db= 25 - 50 cm^2 yr^{-1}) (Fig. 8b). At low q (q≤10 cm yr^{-1}) the activation of bioturbation activity, as well as its intensity exert no impact on the amount of carbonate precipitated, because SR is always located within the bioturbated zone and efficiently dissolves all of the sedimentary calcite there (see section 3.2.2), while the SMTZ is located below the bioturbated interval and thus the precipitation of authigenic carbonates is not affected by bioturbation. In contrast, high fluid flow velocities (q>10 cm yr^{-1}) push the SMTZ into the bioturbated layer and the FCH_4-$CaCO_3$ relationship thus becomes sensitive to the presence of bioturbating organisms. Maximum AOM rates are simulated at the bottom of the bioturbated zone and bioturbation transports authigenic carbonates up in the dissolution zone, reducing the amount of authigenic carbonate by about 30% if bioturbating

organisms are active (Fig. 8b). However, the intensity of this bioturbating activity (i.e. a doubling of Db) exerts no noticeable influence on the amount of carbonate precipitated.

To conclude, although the presence / absence of bioturbating organisms may impact the amount of seep carbonate precipitated, the order of magnitude remains unaltered and bioturbation activity can thus be considered as a second order control on the use of seep carbonate as proxy for CH4 flow.

Sensitivity to bioirr

Bioirrigation enhances the transport of pore water species such as SO_4 or CH_4 across the sediment-water interface. This process thus affects the location and thickness of the SMTZ, as well as the efficiency of the AOM CH_4 sink (Puglini et al., 2020). However, model results indicate that bioirrigation exerts a limited effect on FCH_4-$CaCO_3$ relationship. It is only at very high q values (>50 cm yr^{-1}) that bioirrigation exerts a noticeable impact. This regime pushes the SMTZ close to the sea floor and widens it partially below the bioturbated zone, leaving more time for calcite to precipitate.

In summary, model results reveal that, under the steady-state conditions, the FCH_4-$CaCO_3$ relationship and, thus, the use of seep carbonates as proxies for CH_4 flow benefits from a good knowledge of water depths and sedimentation rates. Yet, it is only weakly sensitive to the value of k_{AOM}, as well as the presence or absence of benthic macro-fauna and largely insensitive to their activity, indicating that weakly constrained parameters do not compromise the use of the model.

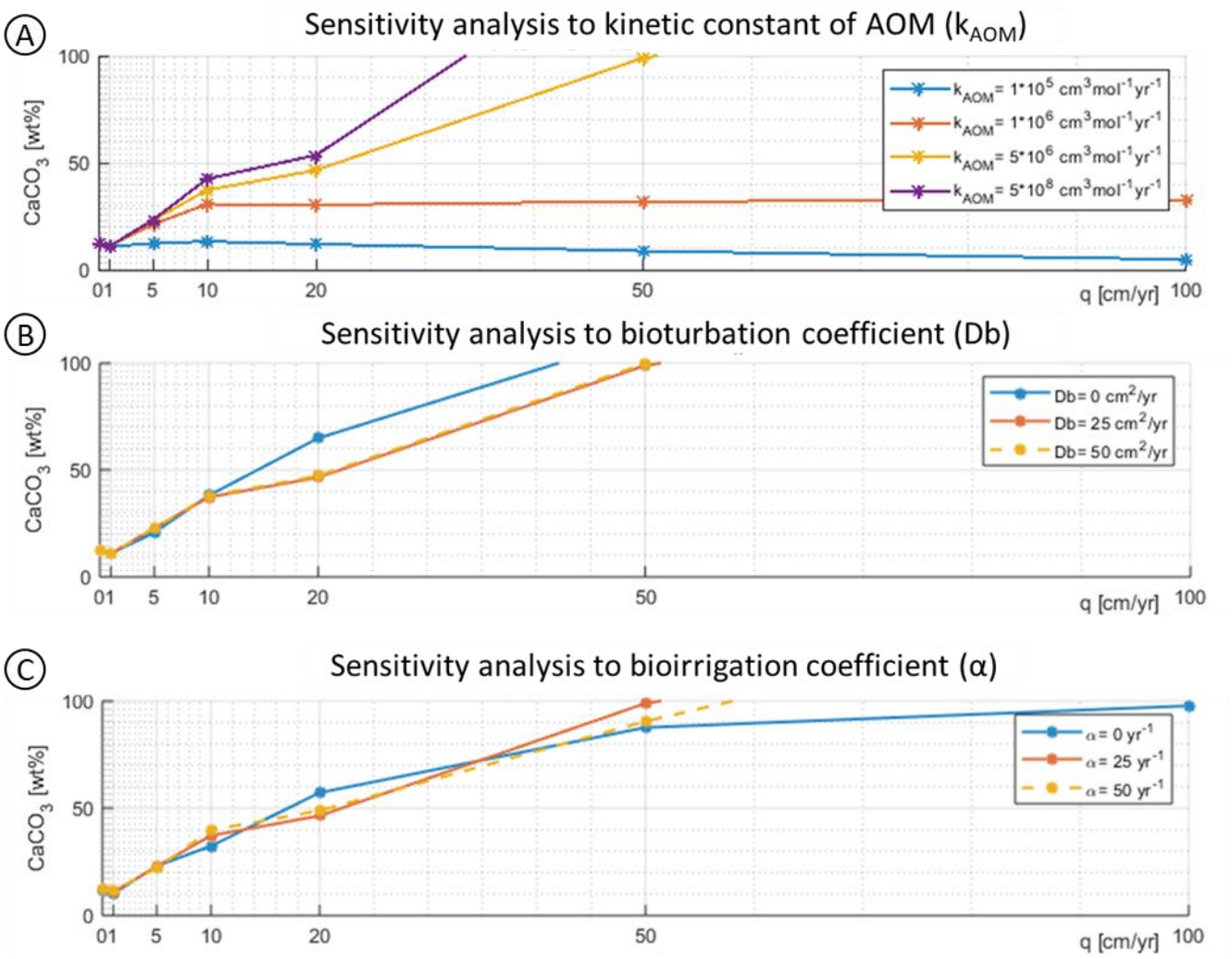

Fig 8: Amount of $CaCO_3$ at the bottom of the model as a function of upward fluid flow (q) for several values of A) kinetic constants of AOM (k_{AOM}); B) bioturbation coefficient (Db); and C) bioirrigation coefficient (α). Any parameter but the studied one is kept constant at a mean value (table 5).

4. Model limitations

Models are simplified representations of natural systems that are too complex to easily understand. It includes all processes essential to the problem, and neglect the others. In what follows, we discuss the most important model limitations and their effects on the applicability of the model-derived FCH_4-$CaCO_3$ relationship.

4.1. Spatial heterogeneities

The precipitation of seep carbonates may induce important heterogeneities in the sediment. First, cementation usually takes place locally, forming discontinuous concretions. Once cemented, concretions deviate the fluid flow laterally without sealing the seep site (Hovland 2002; Agirrezabala

et al. 2013; Blouet et al. submitted), thus allowing for a sub-vertical staking of seep carbonates (Ho et al., 2012; Gay et al., 2019; Blouet et al., accepted). As such, accounting for the reduction of porosity by carbonate cementation would result in a rather unrealistic plugging of the fluid pathway in the 1D model (e.g. Luff and al., 2005); the effect on porosity of calcite precipitation/dissolution is therefore not implemented. The physical 1D model scope should thus rather be seen as a simulation along a curvilinear axis following a flow path rather than a straight vertical axis. Tubular concretions represent another type of heterogeneity. They are sometimes referred to as 'chimneys' in the literature (e.g. De Boever et al., 2006; Magalhães et al., 2012; Angeletti et al., 2015;) and likely correspond to cemented preferred fluid migration pathways (Aiello, 2005; Blouet et al., 2017; Blouet et al., submitted). Such conduits are likely to induce fluid convection in the shallow sediment that triggers lateral inflow into the migration conduit. This lateral inflow locally enhances AOM by supplying additional SO_4^{2-} (Henry et al., 1992, 1996; O'Hara et al., 1995; Aloisi et al., 2004; Santos et al., 2012). Because our model approach does not account for such lateral supply of reactants, model results can thus not be directly applied to tubular concretions. Furthermore, open conduits may also serve as migration pathway for gas bubbles, instantly rising up to the sea floor and by-passing the SMTZ (Haeckel et al., 2007). Our model results therefore preferentially apply to poorly focused seep sites, without evidences of gas bubbling.

4.2. Temporal heterogeneities

The presented model study considers steady state conditions. Although transient phenomena are not explicitly simulated in the model, the sensitivity analysis on the kinetic constant of AOM (k_{AOM}) provides some insights into the effect of transient dynamics on seep carbonates as proxies for fluid flow. Sensitivity tests reveal that the slow growth rate of the local AOM community results in a lagged response of seep carbonate precipitation to changing environmental conditions (Nauhaus et al, 2007; Dale et al., 2008, Puglini et al., 2020). As a consequence, sudden fluid burst over daily to monthly time scales, triggered by fluid migration mechanisms in the deep subsurface and the shallow sea floor (e.g. Sibson et al., 1981, Leifer et al., 2004. Tryon and Brown, 2004; Saffer and Tobin, 2011), cannot be recorded by seep carbonates. Most significantly, catastrophic events like slope failure or pockmark eruption may trigger CH_4 fluxes that are several orders of magnitude larger than those observed under steady fluid flow conditions (Hovland, 1989; Judd and Hovland, 2009; Kramer et al., 2017). While not recorded by seep carbonates, such event may be detected by sea floor topography analysis, highlighting the need for an integrated approach to qualitatively reconstruct fluid flow over geological time scales.

Sedimentation is by nature a transient phenomenon and sedimentation rate measurements typically average periods of sediment accumulation and periods of non-deposition (i.e. erosion,

hiatuses). It is established that the coarser the temporal resolution of these measurements, the longer is the period of these hiatuses and the larger the thickness of the eroded intervals. As a consequence, sedimentation rates measured over shorter time periods are systematically faster than those measured over longer periods (Schumer et al., 2009). According to Sadler (1981, 1991, 1999) the typical baseline continental slope sedimentation rate applied here (i.e. w=0.1 cm/yr) is equivalent to an apparent steady state sedimentation rate of 0.01 cm/yr if actually measured on a 10^2yr timescale, and 0.0001 cm/yr if measured on a 10^6yr timescale. Given that the shortest variations in CH_4 flux that can be captured by seep carbonates are determined by the slow growth of the microbial AOM community, sedimentation rates should ideally be integrated over decadal time scales. However, such a resolution is almost unreachable in the fossil record, and may induce uncertainty to the quantitative application of the model in the past.

4.3. Maximization of the amount of calcite

Perhaps no aspect of carbonate diagenesis is more controversial than the values of rate constants of precipitation and dissolution and minimal saturation threshold at which carbonate minerals start to precipitate (Morse, 2003; Boudreau 2013). Using high values for the kinetic rate constants and an oversaturation threshold of 1, our model most probably overestimates the actual rates of precipitation and dissolution. The amounts of calcite precipitated at seep sites are therefore maximized in our simulations.

4.4. Sea water composition

The composition of sea water defined in our model corresponds to the one of the modern global ocean. However, its chemical composition has significantly evolved over time and our results should thus be extrapolated with care if applied to other geological periods. For example, the concentration of sulfate was about a third of its modern value during the early Cretaceous (Antonelli et al., 2017). Exploring the effect of changing sea water composition on the FCH_4-$CaCO_3$ relationship is beyond the scope of the present study but should be explored in future research.

5. Model applications to observational data

To illustrate how our model results can be applied to interpret observational data, we 1) infer the growth rate of concretions from rates of seep carbonate precipitation and 2) reconstruct past CH_4 fluxes and their environmental controls from seep carbonates observed in seismic data

5.1. Growth rate of concretions

The depth-integrated rate of calcite precipitation can be used to approximate the time needed to precipitate a carbonate concretion for different q values (Table 7). Assuming a full authigenic $CaCO_3$ cementation (0% porosity; 15% detrital grains content; calcite density 2.7 g/cm^3), the growth rate of concretions increases by a factor of 35 over the range of fluid flow regimes investigated here (i.e. from 0.4 cm/kr to 14 cm/kr at a water depth of 200 m). An increase in water depth (1000 m) leads to a reduction in the time required to form concretions, as well as an increased sensitivity to fluid flow. We find that at 1000 m the growth of a concretion is 7.5 cm/kyr for q= 10 cm/yr, a value comparable to the one calculated by Luff and Wallmann (2003) at Hydrate Ridge, 4.5 cm/kyr (750 m water depth, q = 10 cm yr^{-1}). Based on U-Th dating, Bayon et al. (2009) measured the growth rates of multilayered carbonates crusts from the Nil deep-sea fan (1650 m water depth) comprised between 0,4 - 5 cm/kyr. This crust being composed of 90% $CaCO_3$, with a bulk density of 1,6 g/cm^3 due to the presence of large vugs, the equivalent growth rates for a fully cemented carbonate crust would be comprised between 0,2 - 3 cm/kyr. Our simulations results suggest that the steady state fluid flow needed to grow such crusts is on the order of a few centimeters per year.

5.2. Reconstructing CH_4 flux from seismic observation of seep carbonates

Traditionally, the ages and growth rates of seep carbonates are considered to be solely related to the CH_4 supply. Therefore, they are often used as a tracer for changes in fluid flow intensity only (Liberteau et al., 2005, 2006; Cremière et al., 2016), thus overlooking the potentially important role of changes in sedimentation rate and water depth that has been identified in our study. The model results presented in this study provide a quantitative framework that potentially allows for a more holistic and quantitative assessment of the major processes controlling seep carbonate precipitation. We illustrate this holistic approach on the basis of a classical example of a vertical stack of amplitude anomalies, interpreted as seep carbonates, observed on seismic data in hemipelagic sediments in the Plio-pleistocene offshore Angola (1300 m water depth) by Ho et al. (2012). Eustatic variations merely reach an order of magnitude of 100 m over the Plio-pleistocene (Haq et al., 1987) and thus represent only ca. 10% of the total water depth (1300 m). Therefore, these variations can be ruled out as a first order factor control on the fluctuations in seep carbonate cementation in this case study. Seep carbonates must thus be related to changes in fluid flow, as suggested by Ho et al. (2012) and the present study, or, alternatively, to changes in sedimentation rate, as suggested by our model results. The lack of calibration between seismic amplitude and carbonate content and the lack of detailed information on sedimentation rate prevents a fully quantitative reconstruction of past CH_4 flow. We thus only attempt a qualitative assessment of the potential factors that drove the observed, vertical evolution seep carbonate cementation in this ca. 100 m in diameter, 300 m thick column..

The sequence of amplitude anomalies starts with a pockmark: the depression cross cut the stratigraphy, demonstrating its erosive origin probably associated with a massive and brutal eruption of fluids (Hovland 1989; Judd and Hovland 2007; Kramer et al., 2017). According to our model results, the eruption has left no trace in the seep carbonate record due to the delayed microbial response to abrupt changes in the fluid flow regime. The pockmark is followed by two stacks of seep carbonate vertically separated by a weakly cemented interval, which Ho et al (2012) interpreted as two sequences of seepage interrupted by a dormant stage. This explanation is plausible but our model results suggest that a sequence of seep carbonates, such as the one observed here, can also be related to changes in sedimentation rate. Interestingly, the weakly cemented interval is associated with a rather homogenous amplitude domain in the seismic record, indicating a relatively homogeneous lithology, and is capped by a high amplitude reflector, which marks a significant lithology change. Assuming that sediment lithology is related to sedimentation rate, the weakly cemented interval may correspond to a period of relatively high sedimentation rate. The change in lithology that follows may in turn correspond to a relative slowdown in sedimentation rate.

In summary, the reactive-transport model established here CH_4provides a quantitative and interpretative framework that allows to 1) test alternative environmental scenarios that might lead to the observed sequence in the seismic record; 2) identify the key environmental variables that need to be constrained and, once constrained; 3) quantify first-order estimates of past CH_4 flow, taking into account the limits of applicability of our model. For instance, a detailed analysis of sedimentation rates over the considered vertical stack of amplitude anomalies (which is outside the scope of this study) would help identify the main control on carbonate precipitation. If sedimentation rate remains relatively constant over the considered interval, past variations in methane flux likely exerted the dominant control on seep carbonate precipitation. In contrast, if significant variations in sedimentation rate are observed, it is likely that seep carbonate precipitation is controlled by these variations. In both cases, knowledge of sedimentation rate would allow for a first-order quantitative reconstruction of past CH_4 fluxes based on the quantitative framework developed here.

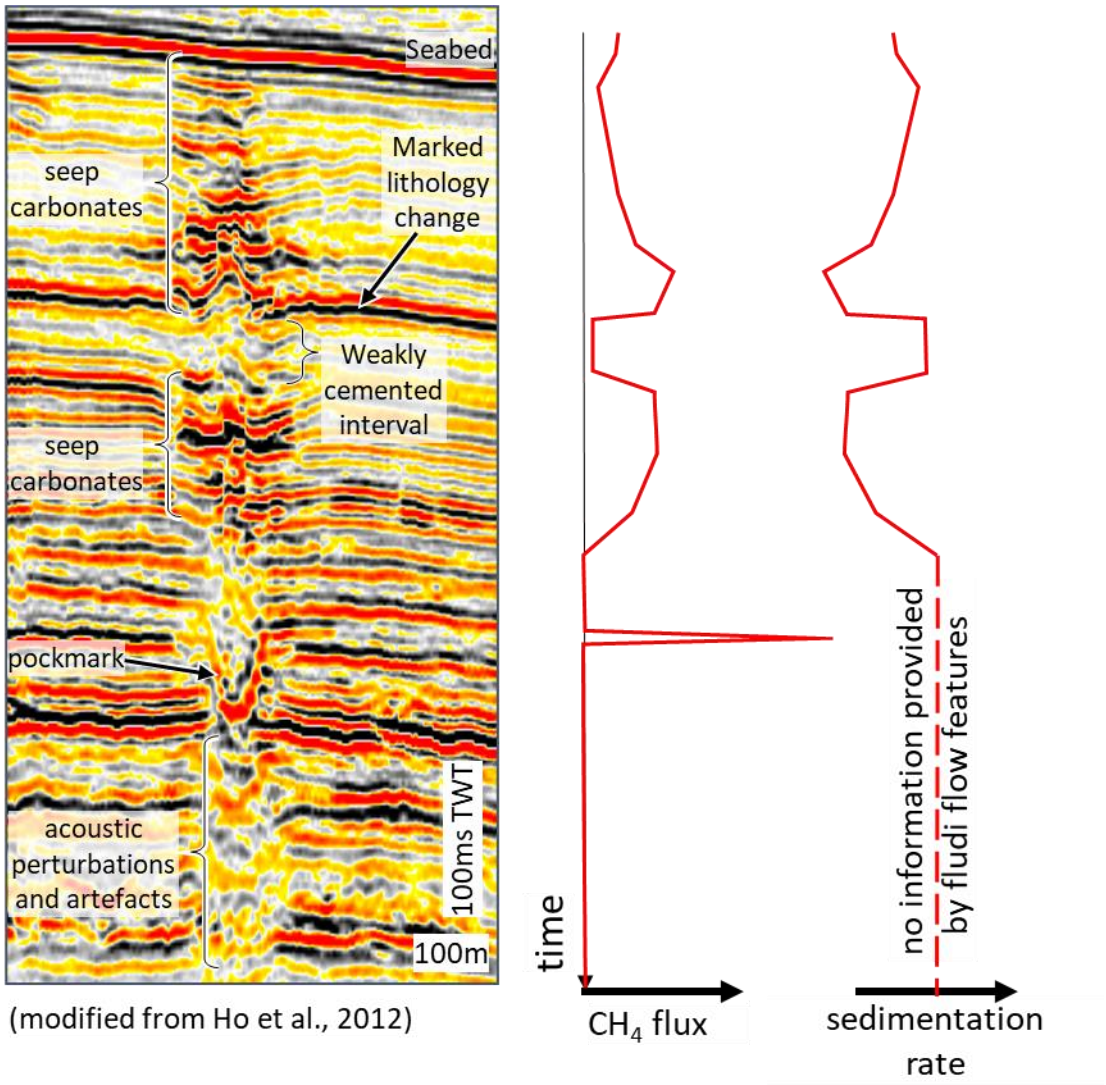

Figure 9: Vertical succession of a pockmark and two sub-circular amplitude anomalies stacks interpreted by Ho et al. (2012) as seep carbonates (left). The middle panel interprets the vertical variability of seep carbonate cementation to a temporal evolution of CH_4 flux, as suggest by Ho et al. (2012). The right panel interprets the same sequence as a result of variations in sedimentation rates.

6. Conclusion

We used a one-dimensional reaction-transport model (RTM) to evaluate the extent to which seep carbonates can be used as proxies for CH_4 flow through marine sediments. This was achieved by first developing a theoretical framework that can relate organoclastic sulfate reduction and anaerobic oxidation of CH_4 (AOM) to associated pH changes and carbonate precipitation and then identifying the dominant environmental drivers of the coupled C-S cycles in seep environments. We found that it is indeed possible to use the amount of seep carbonate as a quantitative indicator for CH_4 leakage over a wide range of environmental conditions encountered at seep sites. In particular CH_4 flux almost linearly scales to the amount of precipitated carbonate ($nCH_4 = 3.3\text{-}5.2\ nCaCO_3$)

within a “quantitative domain” from low to moderate fluid flows. At higher fluid flows, full cementation generally impedes direct quantitative CH4 flux estimates. Yet, within this “threshold domain”, the minimum CH_4 flux required for full cementation still provides a lower bound estimate of CH_4 flux. In addition, and in contrast to the traditional view of CH_4 flux as the dominant control on seep carbonate precipitation, we showed that sedimentation rate (w) and water depth also exert an important control on the amount of carbonate precipitated mainly via their effects on residence time and CH_4 solubility, respectively. As a consequence, vertical variations of the degree of cementation of staked seep carbonates bodies might indicate not only temporal changes in fluid flow, but also changes in sedimentation rate and/or water depth. Furthermore, our results reveal environmental factors that are difficult to constrain, such as benthic macrofaunal activity and the kinetic rate constant of AOM generally exert no significant impact on the relationship between the CH_4 flux and the amount of carbonate precipitated. A notable exception corresponds to a case of very low AOM kinetic rate constants that are typically indicative of low AOM biomass as found in, for instance, passive settings or under highly transient conditions when the AOM biomass cannot adapt to abrupt changes in fluid flow regimes. Here, low AOM rates severely limit carbonate precipitation. Event CH_4 releases characterized by fluid flows possibly several order of magnitude larger than under steady conditions, such as during pockmark eruptions, would not be recorded by seep carbonate precipitation.

7. Acknowledgments

We thank Total Exploration and Production for the financing this project and for many insightful discussions with geoscientists of the sedimentology and geochemistry research teams. Claude Gout is thanks for his long term following up of this problematic.

8. Acknowledgements

Primary Redox Reactions	kinetic rate laws	Ta	Tc	Ts
sulfate reduction $CH_2O(NH_3)_y + ½\ SO_4^{2-} + yH^+ \rightarrow HCO_3^- + ½\ H_2S + yNH_4^+$	$R_{SR} = R_{POC}\, f_{SO_4^{2-}}$	(1+y)	1	1/2
methanogenesis $CH_2O(NH_3)_y + yH^+ \rightarrow ½\ CH4 + ½\ CO_2 + yNH_4^+$	$R_{meth} = R_{POC}(1 - f_{SO_4^{2-}})$	y	1/2	0
Secondary Redox Reactions				
anaerobic oxydation of methane $CH_4 + SO_4^{2-} \rightarrow HCO_3^- + HS^- + H_2O$	$R_{AOM} = k_{AOM}\,[CH_4]\,[SO_4^{2-}]$	2	1	1
Carbonate Precipitation / Dissolution				
carbonate dissolution $CaCO_3 \rightarrow Ca^{2+} + CO_3^{2-}$	$R_{CalDiss} = k_{CalDis}\,[CaCO_3]\,(1 - [Ca^{2+}]\,[CO_3^{2-}] / K_{spCal})$	2	1	0
carbonate precipitation $Ca^{2+} + CO_3^{2-} \rightarrow CaCO_3$	$R_{CalPrec} = k_{CalPrec}\,([Ca^{2+}]\,[CO_3^{2-}] / K_{spCal} - 1)$	-2	-1	0
Equilibrium Conditions	**mass action laws**			
carbonic acid dissociation $H_2CO_3^- = HCO_3^- + H^+$	$R_{eq1} = [H^+]\,[HCO_3^-] / [H_2CO_3^-]$			
bicarbonate dissociation $HCO_3^- = CO_3^{2-} + H^+$	$R_{eq2} = [H^+]\,[CO_3^{2-}] / [HCO_3^-]$			
sulfide dissociation $H_2S = HS^- + H^+$	$R_{eq3} = [H^+]\,[HS^-] / [H_2S]$			
boric acid dissociation $BOH_4 = BOH_3^- + H^+$	$R_{eq4} = [H^+]\,[B(OH)_3^-] / [B(OH)_4]$			
autoprotlysis of water $H_2O = OH^- + H^+$	$R_{eq5} = [H^+]\,[OH^-]$			

Table 1: The reaction network with kinetic rate laws, mass action laws and stoichiometric coefficients of total dissolved inorganic carbon (Tc), total alkalinity (Ta), and total sulfides (Ts) for each kinetic reaction. y=16/106

parameter	value					units	reference
$f_{SO_4^{2-}}$	1 for $[SO_4^{2-}] > km_{SO_4^{2-}}$					-	
$f_{SO_4^{2-}}$	$[SO_4^{2-}]/km_{SO_4^{2-}}$ for $[SO_4^{2-}] \leq km_{SO_4^{2-}}$					-	
$km_{SO_4^{2-}}$	$1 * 10^{-6}$					mol cm^{-3}	Van Cappellen and Ingall (1996)
nu	0,125					-	Arnd et al. (2013)
a	10					yr	Arnd et al. (2013)
k_{AOM}	Cf. Table 5					cm^3 mol^{-1} yr^{-1}	
$k_{CalDiss}$	1					yr^{-1}	Luff and wallmann (2003)
$k_{CalPrec}$	0,1					mol cm^3 yr	Luff and wallmann (2003)
parameter	**value for a gien water deph**					**units**	
	10 m	100 m	200 m	500 m	1000 m		
k_{spCal}	$4,32 * 10^{-13}$	$4,40 * 10^{-13}$	$4,48 * 10^{-13}$	$4,47 * 10^{-13}$	$5,19 * 10^{-13}$	mol^2 cm^{-6}	Millero (1995)
R_{eq1}	$0,99 * 10^{-9}$	$1,00 * 10^{-9}$	$1,01 * 10^{-9}$	$1,04 * 10^{-9}$	$1,1 * 10^{-9}$	mol cm^{-3}	Millero (1995)
R_{eq2}	$6,37 * 10^{-13}$	$6,41 * 10^{-13}$	$6,46 * 10^{-13}$	$6,6 * 10^{-13}$	$6,82 * 10^{-13}$	mol cm^{-3}	Millero (1995)
R_{eq3}	$1,72 * 10^{-10}$	$1,75 * 10^{-10}$	$1,80 * 10^{-10}$	$2,13 * 10^{-10}$	$3,8 * 10^{-10}$	mol cm^{-3}	Millero (1995)
R_{eq4}	$1,65 * 10^{-12}$	$1,67 * 10^{-12}$	$1,69 * 10^{-12}$	$1,75 * 10^{-12}$	$1,86 * 10^{-12}$	mol cm^{-3}	Millero (1995)
R_{eq5}	$1,40 * 10_{-20}$	$1,4 * 10^{-19}$	$1,42 * 10^{-20}$	$1,47 * 10^{-20}$	$1,55 * 10^{-20}$	mol^2 cm^{-6}	Millero (1995)

Table 2: Parameters of the reaction network

Species i	molecular diffusion coefficient at 0°C Di0 [cm^2/yr]	temperature dependence of diffusion coefficient fT [$°C^{-1}$]
CH_2O	0	0
SO_4^{2-}	173,9	0,045
CH4	263,9	0,052
H_2S	331,6	0,06
HS^-	392	0,031
$B(OH)_4^-$	96,3	0,048
$B(OH)_3$	110	0,048
H_+	600	0,06
$CaCO_3$	0	0
Ca	150,4	0,045
NH^{4+}	395,8	0,041
H_2CO_3	320	0,06
HCO_3^-	217,2	0,048
CO_3^{2-}	176,1	0,047
OH^-	600	0,06

Table 3 : Molecular diffusion coefficients for the simulated species (Boudreau, 1997)

Model parameters	value	units
Temperature	10	°C
Salinity	35	g/dm^3
[CH4]sat	28,5 * 10^{-6}	mol/cm^3
sedimentation rate (w)	0,1	cm/yr
bioturbation coefficient at the surface (Db)	Cf. Table 5	cm^2/yr
depth of the bioturbated layer	10	cm
bioirrigation coefficient at the surface (α)	Cf. Table 5	yr^{-1}
Porosity at the surface of the sediment	0,92	-
porosity at great depth	0,8	-
porosity attenuation coefficient	0,15	-
density of solids	2,5	g/cm^3

Upper boundary conditions (∀ water depth)	value	units
F_{CH_2O}	4	wt% of w
	6,66 * 10^{-5}	mol/cm^2/yr
F_{CaCO_3}	15	wt% of w
	3,00 * 10^{-5}	mol/cm^2/yr
pH	7,9	-
Alkalinity	2,30 * 10^{-6}	mol/cm^3
TB	0,42 * 10^{-6}	mol/cm^3
TS	0	mol/cm^3
TC	2,17 * 10^{-6}	mol/cm^3
[SO_4^{2-}]	28,00 * 10^{-6}	mol/cm^3
d[CH_4]/dz	0	mol/cm^4
[Ca]	10,00 * 10^{-6}	mol/cm^3
[NH_4]	0	mol/cm^3
Ω_{Cal}	2,33	-

Lower boundary conditions	value for a given water depth					units
	10 m	100 m	200 m	500 m	1000 m	
d[CH_2O]/dz	0	0	0	0	0	mol/cm^4
d[$CaCO_3$]/dz	0	0	0	0	0	mol/cm^4
pH	6,26	6,26	6,26	6,24	6,2	-
Alkalinity	64,83 *10^{-6}	64,95 *10^{-6}	65,49 *10^{-6}	65,5 *10^{-6}	66,47 *10^{-6}	mol/cm^3
TB	0,39 *10^{-6}	0,39 *10^{-6}	0,39 *10^{-6}	0,39 *10^{-6}	0,39 *10^{-6}	mol/cm^3
TS	15,38 *10^{-6}	15,38 *10-^{6}	15,38 *10^{-6}	15,39 *10^{-6}	15,43 *10^{-6}	mol/cm^3
TC	94,49 *10^{-6}	94,58 *10^{-6}	94,66 *10^{-6}	94,88 *10^{-6}	95,24 *10^{-6}	mol/cm^3
[SO_4^{2-}]	0	0	0	0	0	mol/cm^3
[CH_4]	1,49 *10^{-6}	14,00*10^{-6}	28,30 *10^{-6}	53,5 *10^{-6}	214 *10^{-6}	mol/cm^3
[Ca^{2+}]	6,011 *10^{-6}	0,613 *10^{-6}	6,25 *10^{-6}	6,7078 *10^{-6}	7,9 *10^{-6}	mol/cm^3
[NH_4^+]	182,4 * 10^{-6}	182,4 * 10^{-6}	182,4 *10^{-6}	182,4 *10^{-6}	182,4 *10^{-6}	mol/cm$_3$
Ω_{Cal}	1	1	1	1	1	-

Table 4: Model parameters for the transport and boundary conditions of our reactive-transport model. TC=[$H_2CO_3^-$] + [HCO_3^-] + [CO_3^{2-}]; TB = [BOH_4] + [BOH_3^-]; TS= [H_2S] + [HS^-] and Alkalinity = [HCO_3^-] + 2*[CO_3^{2-}] + [HS^-] + [BOH_3^-] +[OH^-] – [H^+]. For more information about the determination of TC and Ω_{cal} at the upper boundary of the model domain, see text.

parameter	value for a given fluid flow velocity (q) (cm yr^{-1})						units
	0	5	10	20	50	100	
coefficient at the surface (Db)	25	100	25	0	0	0	$cm^2\ yr^{-1}$
coefficient at the surface (α)	1	50	20	0	0	0	yr^{-1}
kinetic constant of AOM (k_{AOM})	$1{,}00 * 10^5$	$1{,}35 * 10^6$	$2{,}70 * 10^6$	$5{,}40 * 10^6$	$1{,}35 * 10^7$	$2{,}70 * 10^7$	$cm^3\ mol^{-1}\ yr^{-1}$

Table 5: parameters values of the baseline model as a function of the fluid flow velocity.

parameter	values tested in the sensitivity study				Units
k_{AOM}	$5 * 10^4$	$1 * 10^6$	**$5 * 10^6$**	$5 * 10^8$	$cm^3\ mol^{-1}\ yr^{-1}$
Db	0	**25**	50		$cm^2\ yr^{-1}$
α	0	**25**	50		yr^{-1}

Table 6: Selected values for the sensitivity tests, keeping all parameter but the studied one constant to an arbitrary medium value, highlighted in bold.

9. References

Agirrezabala, L. M. (2009) Mid-Cretaceous hydrothermal vents and authigenic carbonates in a transform margin, Basque-Cantabrian Basin (western Pyrenees): a multidisciplinary study. *Sedimentology,* 56**,** 969-996.

Agirrezabala, L. M. (2015) Syndepositional forced folding and related fluid plumbing above a magmatic laccolith: Insights from outcrop (Lower Cretaceous, Basque-Cantabrian Basin, western Pyrenees). *Geological Society of America Bulletin***,** B31192. 1.

Aguilera, D., P. Jourabchi, C. Spiteri & P. Regnier (2005) A knowledge-based reactive transport approach for the simulation of biogeochemical dynamics in Earth systems. *Geochemistry, Geophysics, Geosystems,* 6.

Aiello, I. W. (2006) Tectonics, Sedimentation and Fluid Flow in Northern Santa Cruz County and Point Reyes. *Field Trip Guide*.

Akam, S. A., R. B. Coffin, H. A. N. Abdulla & T. W. Lyons (2020) Dissolved Inorganic Carbon Pump in Methane-Charged Shallow Marine Sediments: State of the Art and New Model Perspectives. *Frontiers in Marine Science,* 7.

Aloisi, G., K. Wallmann, S. M. Bollwerk, A. Derkachev, G. Bohrmann & E. Suess (2004) The effect of dissolved barium on biogeochemical processes at cold seeps. *Geochimica et Cosmochimica Acta,* 68**,** 1735-1748.

Angeletti, L., S. Canese, F. Franchi, P. Montagna, J. Reitner, E. O. Walliser & M. Taviani (2015) The "chimney forest" of the deep Montenegrin margin, south-eastern Adriatic Sea. *Marine and Petroleum Geology,* 66**,** 542-554.

Antonelli, M. A., N. J. Pester, S. T. Brown & D. J. DePaolo (2017) Effect of paleoseawater composition on hydrothermal exchange in midocean ridges. *Proceedings of the National Academy of Sciences,* 114**,** 12413-12418.

Arndt, S., P. Regnier, Y. Goddéris & Y. Donnadieu (2011) GEOCLIM reloaded (v 1.0): a new coupled earth system model for past climate change. *Geoscientific Model Development,* 4**,** 451-481.

Barry, J., R. Kochevar & C. Baxter (1997) The influence of pore-water chemistry and physiology on the distribution of vesicomyid clams at cold seeps in Monterey Bay: Implications for patterns of chemosynthetic community organization. *Limnology and Oceanography,* 42**,** 318-328.

Berner, R. A. 1980. *Early diagenesis: a theoretical approach*. Princeton University Press.

Blouet, J.-P., P. Imbert & A. Foubert (2017) Mechanisms of biogenic gas migration revealed by seep carbonate paragenesis, Panoche Hills, California. *AAPG Bulletin,* 101**,** 1309-1340.

Blouet, J.-P., P. Imbert, A. Foubert, S. Ho & G. Dupond (accepted) From seep carbonates down to petroleum systems: an outcrop study from the SE France basin. *AAPG bulletin*.

Boetius, A., K. Ravenschlag, C. J. Schubert, D. Rickert, F. Widdel, A. Gieseke, R. Amann, B. B. Jørgensen, U. Witte & O. Pfannkuche (2000) A marine microbial consortium apparently mediating anaerobic oxidation of methane. *Nature,* 407**,** 623-626.

Boudreau, B. P. & B. R. Ruddick (1991) On a reactive continuum representation of organic matter diagenesis. *american Journal of Science,* 291**,** 507-538.

Burton, E. A. (1993) Controls on marine carbonate cement mineralogy: review and reassessment. *Chemical Geology,* 105**,** 163-179.

Chien, C.-W., C.-Y. Huang, S.-D. Min, S.-Y. Jiang, L. Chenhui & Y. Kenn-Ming (2018) Calcareous and agglutinated foraminifera ratio: Chemical interface tracer for Pliocene Chiahsien Paleoseep, SW Taiwan. *TAO: Terrestrial, Atmospheric and Oceanic Sciences,* 29**,** 4.

Crémière, A., A. Lepland, S. Chand, D. Sahy, D. J. Condon, S. R. Noble, T. Martma, T. Thorsnes, S. Sauer & H. Brunstad (2016) Timescales of methane seepage on the Norwegian margin following collapse of the Scandinavian Ice Sheet. *Nature communications,* 7.

Dale, A. W., V. Brüchert, M. Alperin & P. Regnier (2009) An integrated sulfur isotope model for Namibian shelf sediments. *Geochimica et Cosmochimica Acta,* 73**,** 1924-1944.

Dale, A. W., P. Regnier, N. J. Knab, B. B. Jørgensen & P. Van Cappellen (2008) Anaerobic oxidation of methane (AOM) in marine sediments from the Skagerrak (Denmark): II. Reaction-transport modeling. *Geochimica et Cosmochimica Acta,* 72**,** 2880-2894.

Dale, A. W., P. Regnier & P. Van Cappellen (2006) Bioenergetic controls on anaerobic oxidation of methane (AOM) in coastal marine sediments: a theoretical analysis. *American Journal of Science,* 306**,** 246-294.

De Boever, E., R. Swennen & L. Dimitrov (2006) Lower Eocene carbonate cemented chimneys (Varna, NE Bulgaria): Formation mechanisms and the (a) biological mediation of chimney growth? *Sedimentary Geology,* 185**,** 159-173.

Fischer, D., H. Sahling, K. Nöthen, G. Bohrmann, M. Zabel & S. Kasten (2012) Interaction between hydrocarbon seepage, chemosynthetic communities, and bottom water redox at cold seeps of the Makran accretionary prism: insights from habitat-specific pore water sampling and modeling. *Biogeosciences,* 9**,** 2013-2031.

Gallagher, K. L., C. Dupraz & P. T. Visscher (2014) Two opposing effects of sulfate reduction on carbonate precipitation in normal marine, hypersaline, and alkaline environments: COMMENT. *Geology,* 42**,** e313-e314.

Gay, A., M. Lopez, J.-L. Potdevin, V. Vidal, G. Varas, A. Favier & N. Tribovillard (2018) 3D morphology and timing of the giant fossil pockmark of Beauvoisin, SE Basin of France. *Journal of the Geological Society***,** jgs2018-064.

Haeckel, M., B. P. Boudreau & K. Wallmann (2007) Bubble-induced porewater mixing: A 3-D model for deep porewater irrigation. *Geochimica et Cosmochimica Acta,* 71**,** 5135-5154.

Hecker, B. (1985) Fauna from a cold sulfur-seep in the Gulf of Mexico: comparison with hydrothermal vent communities and evolutionary implications. *Bulletin of the biological Society of Washington***,** 465-473.

Henry, P., J.-P. Foucher, X. Le Pichon, M. Sibuet, K. Kobayashi, P. Tarits, N. Chamot-Rooke, T. Furuta & P. Schultheiss (1992) Interpretation of temperature measurements from the Kaiko-Nankai cruise: Modeling of fluid flow in clam colonies. *Earth and Planetary Science Letters,* 109**,** 355-371.

Henry, P., X. Le Pichon, S. Lallemant, S. Lance, J. B. Martin, J. P. Foucher, A. Fiala-Médioni, F. Rostek, N. Guilhaumou & V. Pranal (1996) Fluid flow in and around a mud volcano field seaward of the Barbados accretionary wedge: results from Manon cruise. *Journal of Geophysical Research: Solid Earth,* 101**,** 20297-20323.

Ho, S., D. Carruthers & P. Imbert (2016) Insights into the permeability of polygonal faults from their intersection geometries with Linear Chimneys: a case study from the Lower Congo Basin. *Carnets Geol.,* 16**,** 17.

Ho, S., J. Cartwright & P. Imbert. 2012. The formation of advancing pockmarks arrays: an interplay between hydrocarbon leakage and slope sedimentation. In *Abstracts, American Association of Petroleum Geologists Annual Convention and Exhibition. Long Beach, USA*, 22-25.

Ho, S., M. Hovland, J.-P. Blouet, A. Wetzel, P. Imbert & D. Carruthers (2018a) Formation of linear planform chimneys controlled by preferential hydrocarbon leakage and anisotropic stresses in faulted fine-grained sediments, offshore Angola. *Solid Earth,* 9.

Ho, S., P. Imbert, M. Hovland, A. Wetzel, J.-P. Blouet & D. Carruthers (2018b) Downslope-shifting pockmarks: interplay between hydrocarbon leakage, sedimentations, currents and slope's topography. *International Journal of Earth Sciences***,** 23 p.

Hovland, M. (1989) The formation of pockmarks and their potential influence on offshore construction. *Quarterly Journal of Engineering Geology and Hydrogeology,* 22**,** 131-138.

Hülse, D., S. Arndt, S. Daines, P. Regnier & A. Ridgwell (2018) OMEN-SED 1.0: a novel, numerically efficient organic matter sediment diagenesis module for coupling to Earth system models. *Geoscientific Model Development,* 11**,** 2649-2689.

Joye, S. B., A. Boetius, B. N. Orcutt, J. P. Montoya, H. N. Schulz, M. J. Erickson & S. K. Lugo (2004) The anaerobic oxidation of methane and sulfate reduction in sediments from Gulf of Mexico cold seeps. *Chemical Geology,* 205**,** 219-238.

Judd, A. & M. Hovland (2007) Seabed fluid flow—the impact on geology, Biology and the Marine Environment. *Cambridge University Press***,** 475.

Juniper, S. K. & M. Sibuet (1987) Cold seep benthic communities in Japan subduction zones: Spatial organization, trophic strategies and evidence for temporal evolution. *Marine ecology progress series. Oldendorf,* 40**,** 115-126.

Kaczmarek, S. E., J. M. Gregg, D. L. Bush, H. G. Machel & B. W. Fouke (2017) Dolomite, very hight-magnesium calcite, and microbes - Implications for the Microbial Model of Dolomitization. *SEPM special publication* 109 14.

Karaca, D., C. Hensen & K. Wallmann (2010) Controls on authigenic carbonate precipitation at cold seeps along the convergent margin off Costa Rica. *Geochemistry, Geophysics, Geosystems,* 11.

Karaca, D., T. Schleicher, C. Hensen, P. Linke & K. Wallmann (2014) Quantification of methane emission from bacterial mat sites at Quepos Slide offshore Costa Rica. *International Journal of Earth Sciences,* 103**,** 1817-1829.

Kiel, S., K. A. Campbell & C. Gaillard (2010) New and little known mollusks from ancient chemosynthetic environments. *Zootaxa,* 2390**,** 26-48.

Kleindienst, S., F.-A. Herbst, M. Stagars, F. Von Netzer, M. Von Bergen, J. Seifert, J. Peplies, R. Amann, F. Musat & T. Lueders (2014) Diverse sulfate-reducing bacteria of the Desulfosarcina/Desulfococcus clade are the key alkane degraders at marine seeps. *The ISME journal,* 8**,** 2029-2044.

Krämer, K., P. Holler, G. Herbst, A. Bratek, S. Ahmerkamp, A. Neumann, A. Bartholomä, J. E. van Beusekom, M. Holtappels & C. Winter (2017) Abrupt emergence of a large pockmark field in the German Bight, southeastern North Sea. *Scientific reports,* 7**,** 1-8.

Lash, G. G. (2018) Significance of stable carbon isotope trends in carbonate concretions formed in association with anaerobic oxidation of methane (AOM), Middle and Upper Devonian shale succession, western New York State, USA. *Marine and Petroleum Geology*.

Leifer, I. & R. K. Patro (2002) The bubble mechanism for methane transport from the shallow sea bed to the surface: A review and sensitivity study. *Continental Shelf Research,* 22**,** 2409-2428.

Levin, L. (2005) Ecology of cold seep sediments: interactions of fauna with flow, chemistry and microbes. *Oceanography and Marine Biology: an annual review,* 43**,** 1-46.

Levin, L. A., W. Ziebis, G. F. Mendoza, V. A. Growney, M. D. Tryon, K. M. Brown, C. Mahn, J. M. Gieskes & A. E. Rathburn (2003) Spatial heterogeneity of macrofauna at northern California methane seeps: influence of sulfide concentration and fluid flow. *Marine Ecology Progress Series,* 265**,** 123-139.

Liebetrau, V., A. Eisenhauer, J. Fietzke, K. Hametner, D. Günther & P. Linke (2005) Deciphering the archive of methane-related venting activity and chemical changes in authigenic carbonates of a cold seep environment. *European Geosciences Union,* Geophysical Research Abstracts, Vol. 7, 10314.

Liebetrau, V., A. Eisenhauer, J. Fietzke, K. Hametner, D. Günther & P. Linke (2006) Cold seep carbonates: Geochemical archives of marine methane emanation and gas-hydrate destabilization. *European Geosciences Union,* Geophysical Research Abstracts, Vol. 8, 09719.

Linke, P., K. Wallmann, E. Suess, C. Hensen & G. Rehder (2005) In situ benthic fluxes from an intermittently active mud volcano at the Costa Rica convergent margin. *Earth and Planetary Science Letters,* 235**,** 79-95.

Luff, R., J. Greinert, K. Wallmann, I. Klaucke & E. Suess (2005) Simulation of long-term feedbacks from authigenic carbonate crust formation at cold vent sites. *Chemical Geology,* 216**,** 157-174.

Luff, R. & K. Wallmann (2003) Fluid flow, methane fluxes, carbonate precipitation and biogeochemical turnover in gas hydrate-bearing sediments at Hydrate Ridge, Cascadia

Margin: numerical modeling and mass balances. *Geochimica et Cosmochimica Acta,* 67**,** 3403-3421.

Luff, R., K. Wallmann & G. Aloisi (2004) Numerical modeling of carbonate crust formation at cold vent sites: significance for fluid and methane budgets and chemosynthetic biological communities. *Earth and Planetary Science Letters,* 221**,** 337-353.

Magalhães, V. H., L. M. Pinheiro, M. K. Ivanov, E. Kozlova, V. Blinova, J. Kolganova, C. Vasconcelos, J. A. McKenzie, S. M. Bernasconi & A. J. Kopf (2012) Formation processes of methane-derived authigenic carbonates from the Gulf of Cadiz. *Sedimentary Geology,* 243**,** 155-168.

Magoon, L. B. & W. G. Dow. 1994. The Petroleum System. In *The Petroleum System From Source to Trap,* eds. L. B. Magoon & W. G. Dow, 3-24. American Association of Petroleum Geologists.

Middelburg, J. J., K. Soetaert & P. M. Herman (1997) Empirical relationships for use in global diagenetic models. *Deep Sea Research Part I: Oceanographic Research Papers,* 44**,** 327-344.

Millero, F. J. (1995) Thermodynamics of the carbon dioxide system in the oceans. *Geochimica et Cosmochimica Acta,* 59**,** 661-677.

Moerz, T., N. Fekete, A. Kopf, W. Brueckmann, S. Kreiter, V. Huehnerbach, D. Masson, D. A. Hepp, M. Schmidt & S. Kutterolf. 2005. Styles and productivity of mud diapirism along the Middle American margin. In *Mud volcanoes, geodynamics and seismicity*, 49-76. Springer.

Morse, J. 2003. *Formation and diagenesis of carbonate sediments*.

Nauhaus, K., M. Albrecht, M. Elvert, A. Boetius & F. Widdel (2007) In vitro cell growth of marine archaeal-bacterial consortia during anaerobic oxidation of methane with sulfate. *Environmental microbiology,* 9**,** 187-196.

O'Hara, S. C. M., P. R. Dando, U. Schuster, A. Bennis, J. D. Boyle, F. T. W. Chui, T. V. J. Hatherell, S. J. Niven & L. J. Taylor (1995) Gas seep induced interstitial water circulation: observations and environmental implications. *Continental Shelf Research,* 15**,** 931-948.

Puglini (2020) Assessing the potential for non-turbulent methane escape from the

East Siberian Arctic Shelf. *Biogeosciences,* 17**,** 3247-3275.

Railsback, L. B. (2006) Some fundamentals of mineralogy and geochemistry. *Department of Geology, University of Georgia, Athens, Georgia***,** 30602-2501.

Regnier, P., A. W. Dale, S. Arndt, D. LaRowe, J. Mogollón & P. Van Cappellen (2011) Quantitative analysis of anaerobic oxidation of methane (AOM) in marine sediments: a modeling perspective. *Earth-Science Reviews,* 106**,** 105-130.

Regnier, P., J. P. O'Kane, C. I. Steefel & J. P. Vanderborght (2002) Modeling complex multi-component reactive-transport systems: towards a simulation environment based on the concept of a Knowledge Base. *Applied Mathematical Modelling,* 26**,** 913-927.

Riboulot, V., P. Imbert, A. Cattaneo & M. Voisset (2019) Fluid escape features as relevant players in the enhancement of seafloor stability? *Terra Nova,* 31**,** 540-548.

Sadler, P. 1999. The influence of hiatuses on sediment accumulation rates. In *GeoResearch Forum*, 15-40.

Sadler, P. M. (1981) Sediment accumulation rates and the completeness of stratigraphic sections. *The Journal of Geology,* 89**,** 569-584.

Saffer, D. M. & H. J. Tobin (2011) Hydrogeology and mechanics of subduction zone forearcs: Fluid flow and pore pressure. *Annual Review of Earth and Planetary Sciences,* 39**,** 157-186.

Santos, I. R., B. D. Eyre & M. Huettel (2012) The driving forces of porewater and groundwater flow in permeable coastal sediments: A review. *Estuarine, Coastal and Shelf Science,* 98**,** 1-15.

Schmidt, M., C. Hensen, T. Mörz, C. Müller, I. Grevemeyer, K. Wallmann, S. Mau & N. Kaul (2005) Methane hydrate accumulation in "Mound 11" mud volcano, Costa Rica forearc. *Marine Geology,* 216**,** 83-100.

Schumer, R. & D. J. Jerolmack (2009) Real and apparent changes in sediment deposition rates through time. *Journal of Geophysical Research: Earth Surface,* 114.

Sibson, R. H. (1981) Fluid flow accompanying faulting: field evidence and models. *Earthquake prediction***,** 593-603.

Søreide, I. & C. H. Whitson (1992) Peng-Robinson predictions for hydrocarbons, CO2, N2, and H2 S with pure water and NaCI brine. *Fluid Phase Equilibria,* 77**,** 217-240.

Talukder, A. R. (2012) Review of submarine cold seep plumbing systems: leakage to seepage and venting. *Terra Nova,* 24**,** 255-272.

Thullner, M., A. W. Dale & P. Regnier (2009) Global scale quantification of mineralization pathways in marine sediments: A reaction transport modeling approach. *Geochemistry, Geophysics, Geosystems,* 10.

Thullner, M. & P. Regnier (2019) Microbial Controls on the Biogeochemical Dynamics in the Subsurface. *Reviews in mineralogy and geochemistry,* 85**,** 265-302.

Tryon, M. D. & K. M. Brown (2004) Fluid and chemical cycling at Bush Hill: Implications for gas and hydrate rich environments. *Geochemistry, Geophysics, Geosystems,* 5.

Tryon, M. D., K. M. Brown & M. E. Torres (2002) Fluid and chemical flux in and out of sediments hosting methane hydrate deposits on Hydrate Ridge, OR, II: Hydrological processes. *Earth and Planetary Science Letters,* 201**,** 541-557.

Tryon, M. D., K. M. Brown, M. E. Torres, A. M. Tréhu, J. McManus & R. W. Collier (1999) Measurements of transience and downward fluid flow near episodic methane gas vents, Hydrate Ridge, Cascadia. *Geology,* 27**,** 1075-1078.

Wallmann, K., M. Drews, G. Aloisi & G. Bohrmann (2006) Methane discharge into the Black Sea and the global ocean via fluid flow through submarine mud volcanoes. *Earth and Planetary Science Letters,* 248**,** 545-560.

***Declaration of Interest Statement**

Declaration of interests

☒ The authors declare that they have no known competing financial interests or personal relationships that could have appeared to influence the work reported in this paper.

☐The authors declare the following financial interests/personal relationships which may be considered as potential competing interests: